Progress in Earth and Planetary Science

RESEARCH ARTICLE Open Access

Bubbles to Chondrites-I. Evaporation and condensation experiments, and formation of chondrules

Yuki Nakano[1*] and Akihiko Hashimoto[2]

Abstract

We propose a simple model of chondrule formation that is supported by our new experiments. With a laser-heating and inert-gas-cooling technique, we obtained evaporation and condensation pathways starting with chondritic compositions till ends, and extracted 'relative volatilities' of elements from them. Above boiling points, we observed numerous silicate droplets being ejected from collapsed cavities of vapor bubbles on the surface of molten sample, known as jet-droplets. We postulate jet-droplets as origin of chondrules. The formation mechanism of jet-droplets requires a dense and large solid body (>3 cm across), named 'duston', for chondrule precursors. Our chondrule formation model presumes dustons having CI-like composition. Upon boiling, a duston ejects jet-droplets from its molten surface and simultaneously forms an adiabatically expanding vapor cloud around it. The jet-droplets supercool and incorporate the supersaturated vapor and fine condensates while they travel through the cloud, thus completing their makeup as chondrules. The compositions and the mixing ratio of the three components (jet-droplet, vapor and condensate) can be exactly predicted by using relative volatilities of elements, given the chondrule composition to be fitted and the conditions: vaporization degree (VD) and redox state (f_S) of the duston. We attempt to reproduce bulk compositions of chondrules in total of 600. About 75% chondrules are successfully matched with specific combinations of VD and f_S for each chondrule. The model altogether explains 3.5 features of chondrules: maximum size and size-frequency distribution; chemical variety; and textural variety.

Keywords: Evaporation, Condensation, Experiment, Chondrule, Chemical fractionation, Boiling, Jet-droplet, Chondrule fromation, Protoplanetary disk, Solar system

Introduction

The present (I) and companion (II) (Hashimoto and Nakano 2020) papers in tandem present a new formation mechanism of chondrules and chondrites, that begins with bursting of silicate vapor bubbles and ends with asteroid formation as chondritic rubble piles: Bubbles to Chondrites.

Chondrules are compact, mm-sized silicate spherules with igneous textures. They are major constituents, 20-80 vol.%, of chondritic meteorites, fragments of bodies in the asteroid belt (e.g., Wood 1988).

A model of chondrule formation must comply with 3.5 fundamental features that characterize chondrules, apart from the fact that they were once molten. 1) They have a maximum size of 1-5 mm in diameter. In addition, their size frequency distributions roughly obey log-normal distributions (e.g., Friedrich et al. 2015). 2) Their chemical compositions are highly variable (e.g., Jones et al. 2005). 3) They exhibit various petrographic textures that may be related to their thermal histories even amongst chondrules with similar compositions (e.g., Hewins 1997). Chondrule formation models advocated so far (many references in Boss 1996; Desch et al. 2012; Connolly and Jones 2016), are mostly concerned with heating mechanism to melt preexisting solids, but do not generally address the above features.

*Correspondence: yudaruma@ep.sci.hokudai.ac.jp
[1]Department of Cosmosciences, Hokkaido University, N10 W8, Sapporo 060-0810, Japan
Full list of author information is available at the end of the article

Astrophysical observations have revealed that a protostar and a protoplanetary disk (PPD) evolve in concert and form from the same source materials, gas and dust of low-temperature origin that evolved from interstellar medium in accord with physical conditions in PPD (e.g., Drain 2003; Natta et al. 2007; Waters 2015). Macroscopic dust aggregates that are random collections of lightly modified interstellar dust grains, originally 0.02-1 μm in size (Kim et al. 1994), will be uniform in bulk chemical composition. Thus, the composition of the source material for chondrules should be identical to the composition of the Sun (except gases) or that of CI chondrites.

Observation of chondrules suggests that four processes, in combination, were involved in establishing the chondrule properties: melting, evaporation, condensation and crystallization (e.g., Hewins 1997). As pointed out by Sears et al. (1996) and Krot et al. (2004), evaporation and condensation are a requisite for bringing about the variation in chondrule composition. Therefore, a study on evaporation and condensation of silicate systems is a key to understanding detailed conditions of chondrule formation.

Evaporative chemical fractionation of chondritic materials has been studied experimentally (Hashimoto et al. 1979; Hashimoto 1983; Floss et al. 1996; Wang et al. 2001; Yu et al. 2003). These experiments provided evaporative fractionation trends, but were of limited applications as their experimental conditions were selective. Nevertheless, they have been extensively used to develop evaporation models that could be applied over a wider range of conditions (e.g., Alexander 2001, 2002; Fedkin et al. 2006, 2012; Fedkin and Grossman 2013). Condensation of the multi-component silicate vapor has not been studied yet. For a comprehensive understanding of chemical fractionations caused by evaporation and condensation, we have built a new experimental apparatus that allows simultaneous investigations of evaporation and condensation.

In "Experimental methods" section, we describe high-temperature boiling experiments on chondritic materials using a CO_2 laser as a heat source. In "Experimental results" section, we investigate two products of the experiments: numerous droplets ejected from the silicate liquids and ultrafine vapor condensates. They define chemical fractionation trajectories caused by evaporation and condensation, from which we extract a new quantity, 'relative volatilities' of elements to be used in the following analyses. In "Jet-droplets as origin of chondrules" section, we show that the droplets are jet-droplets that were ejected from collapsed vapor cavities, and propose jet-droplets as a possible origin of chondrule nuclei. The presence of dense and large (>3 cm across) dust aggregates, 'dustons', in the solar PPD is required for the source of chondrules. In "Origin of chondrule chemistry" section, we propose a new chondrule formation model that considers an interaction of chondrule nuclei with the vapor cloud that enshrouds the duston, while they travel through it. A quantitative analysis of model chondrules thus produced explains real chondrule chemistry. "Origin of other features of chondrules" section shows the consistency of the model with other features of chondrules. "Conclusions" section summarize our works.

Experimental methods

Initial materials

Two initial materials are used in this study: Allende meteorite powder and a synthetic L silicate (hereafter L^{sil}). L^{sil} was prepared by mixing ten chemical reagents in oxide forms (MgO, SiO_2, FeO, $AlO_{1.5}$, CaO, MnO, $CrO_{1.5}$, TiO_2, $NaO_{0.5}$ and $KO_{0.5}$; purity 99 - 99.999%), in their proportions in the silicate phase of the averaged wet-chemical analyses of 54 L chondrites (falls) compiled by Jarosewich (1990). Exceptions were made for $KO_{0.5}$, MnO and TiO_2, whose concentrations were raised on purpose to 0.5-1.0 wt.% from their original concentrations in Jarosewich's compilation, for the sake of better precision in our chemical analyses. The chemical composition of L^{sil} thus produced is shown in Table 1.

From here on, the molar unit for oxides is taken in the form of MO_x, where M is a metallic element and x represents the normal oxidation number as to M, as shown in Table 1. When the mol%, molar concentration, or molar fraction of the element M in a silicate such as L^{sil} is mentioned in this paper, they refer to those values of the oxide MO_x in the silicate.

A pulverized and homogenized powder of Allende meteorite (<5 μm in grain size) of originally a 100 g chunk, prepared by A. H. in the laboratory of the late Dr. Onuma, was used for experiments. We did not chemically analyze the powder and instead used the analysis by Jarosewich (1990) as shown in Table 1, since 100 g are enough to average out possible indigenous heterogeneity in the meteorite (e.g., Stracke et al. 2012).

The powders were pressed into cylindrical shapes and fired for 12 hours at two temperatures in a mixed gas: 1100 °C and H_2/CO_2 = 1 for L^{sil}, and 1000 °C and H_2/CO_2 = 1/2 for Allende. The sintered samples were drilled halfway

Table 1 The bulk chemical compositions of starting materials (mol%)

Material	$NaO_{0.5}$	MgO	$AlO_{1.5}$	SiO_2	$KO_{0.5}$	CaO	TiO_2	$CrO_{1.5}$	MnO	FeO	Total
Allende	0.84	35.19	3.40	32.82	0.04	2.47	0.10	0.39	0.15	24.60	100
L^{sil}	1.82	37.29	2.88	40.98	0.68	2.22	0.78	0.41	0.46	12.48	100

through their central axes and adjusted for their shape and weight to ∼3 mm in height ∼2.3 mm in diameter, and ∼15 mg.

The choice of the two initial materials is explained. Allende meteorite (CV3) has its bulk chemical composition close to that of CI chondrites, and is available in large quantities for experiments. In the wet chemical analyses of chondrites by Jarosewich (1990), L chondrites are by far the largest in the number of analyses (falls). Therefore, we regarded that the average bulk composition of L chondrites was most reliable. Another and important reason is that during the course of evaporation, Si is preferentially lost, and the Si/Mg ratio continues to decrease. The L chondrite has the Si/Mg molar ratio higher than 1. By adopting the L chondrite composition as the initial material, it is possible to investigate the chemical fractionation in a wide range of the Si/Mg scale. The significance of the Si/Mg scale will be clarified in "Experimental results" section.

Using the two different, initial compositions in experiments, we should be able to extract a general rule from their results.

Apparatus

Figure 1 shows the apparatus and the details inside the vacuum chamber. A cw-CO_2 laser (wave length 10.6 μm; 20-210 watts; NIIC model NC-3010-M) and a ZnSe lens with focal distance of 127 mm are used to heat a sample charge with a spot diameter of 1 mm or less. The sample charge is set in the center of the chamber with a Re wire (0.5 mm in diameter) inserted halfway through the charge on the bottom, and backed up by a graphite disk with a 0.5-1 mm space between them. With the aid of a coaxial diode laser, the charge position is aligned beforehand for the CO_2 laser to take aim at it. The Re wire's role is to pin down the melted charge, while the graphite disk prevents the charge from slipping down along the wire by taking advantage of its poor wettability with silicate liquids.

Temperature measurements are made on the laser-irradiated sample surfaces with an automated pyrometer (IMPAC model IS-12; 0.7-1.1 μm; 700-3500 °C; effective spot diameter ∼0.7 mm at the optimum focal length), whose photometric path is off the laser path by an apex angle of 18°. A prism and a fused-quartz window in the photometric path require their absorption corrections, and they are made beforehand.

The stainless-steel chamber (97 mm ID and 310 mm H) is evacuated with a turbomolecular pump (50 Liter s^{-1}) and an oil-free roughing pump, which are connected to the chamber at its rear side in Fig. 1. An Ar gas (99.9% purity) and a H_2 gas (99.99% purity) are introduced into the chamber using precision valves and mass flow control (for H_2) to the total pressure of 0.3 bar (Ar 0.3 bar; H_2 0.01 bar). The ambient gas has three purposes. (1) It prevents the sample charge from boiling until a high temperature

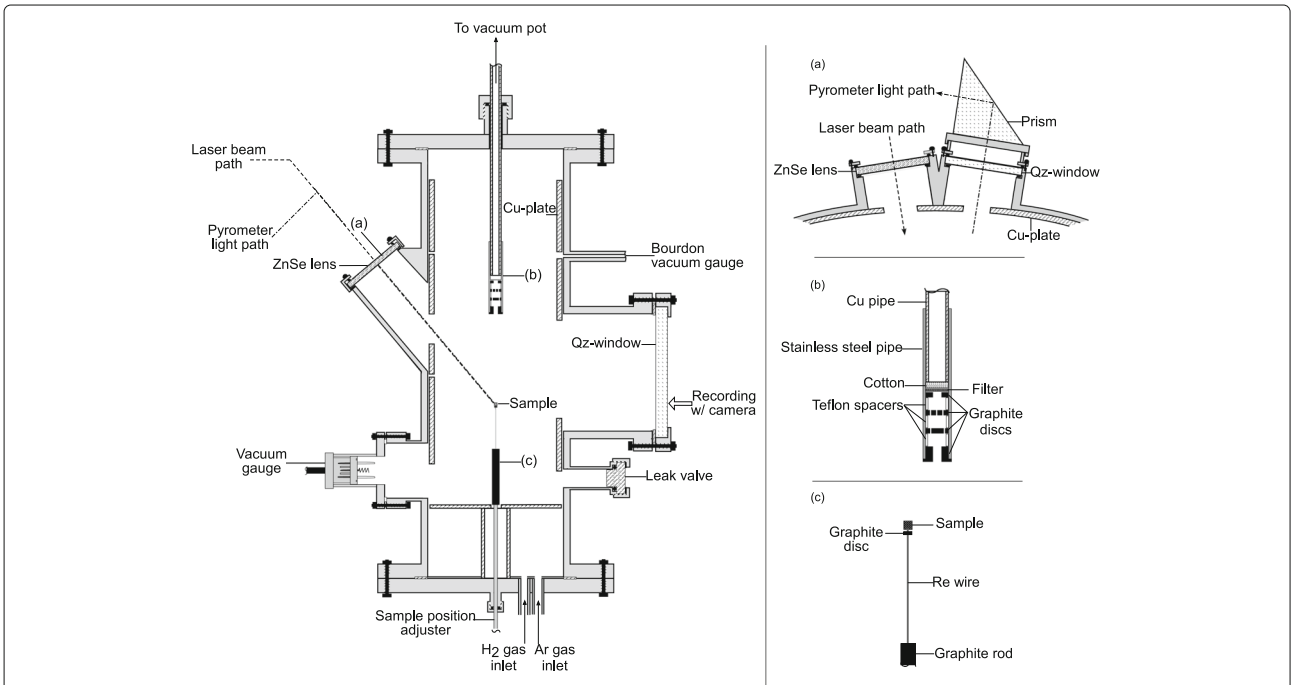

Fig. 1 Schematic diagram of the experimental apparatus. **a** Shows arrangement of the laser and pyrometer light paths. **b** Shows system for collecting condensed particles. **c** Shows sample holding system. Evacuation line is omitted in the diagram

is reached. (2) It regulates the redox condition of the sample charge. (3) It immediately cools the generated vapor and changes the latter into solid condensates, preventing vapor deposition on the chamber wall. The vapor is 100% converted to the solid condensates, that can be recovered at any time. By opening the valve to a vacuum pot, which is connected to the chamber, the condensed particles are collected on a paper filter (7 μm mesh) set in a stainless-steel feedthrough (Fig. 1b).

The ejected silicate droplets from the boiling sample collide with Cu-plates that are set at five positions (top, bottom, front and two sides) inside the chamber, and also collide with the chamber wall where no plate is attached. The droplets are quenched as glasses upon collision with the Cu plate owing to its high thermal conductivity. The chamber wall acts as good as the Cu plate because it is kept cool during the laser heating owing to its large mass.

Throughout the heating experiment, a video camera records scenes covering the area 100 × 70 mm around the sample.

Experimental procedure

The initial masses of the sample charge and of the combined assemblage (sample + Re wire + graphite disk) are weighed with a precision microbalance. The assemblage is set inside the chamber. The vacuum chamber and the vacuum pot are evacuated through separate evacuation lines. When vacuum is reached (10^{-5} Torr) inside the chamber, valves are closed. An H_2 gas is introduced through the mass flow control up to 10^{-2} bar inside the chamber, then Ar is introduced up to 0.3 bar and valves are closed. The pyrometer and video camera are switched on, and the laser heating commences. With a 200W laser power, the sample charge melts completely in ∼0.2 s and starts to boil in ∼0.5 s. After melting, the sample charge keeps its single rounded liquid body; we name it 'Mother Liquid Body' or MLB hereafter. Once boiling starts, numerous droplets are ejected from the MLB in radial directions ("Characteristics of the droplets and the condensed particles" section). The ejection continues until the laser is turned off, or until the boiling stops. The video record indicates their ejection speeds to be 1-3 m s^{-1}, or possibly faster due to the limitation of the conventional video camera.

Often boiling and droplet-ejection stop, as a result of the MLB moving away from the laser focus. Whenever this happens, the MLB is repositioned by manipulating the manual stick connected to the sample assembly as quickly as possible. The pyrometer records the temperature of the MLB at 0.01 s intervals. Unfortunately, however, the pyrometer is too heavy for manual handling and its focal position is adjusted with a two-axis tilt stage, which slows down its realignment. This disadvantage has resulted in the temperature measurement in many experiments to be incomplete.

The moment the laser irradiation commences, a smoke-like haze develops around the sample. The smoke is a sheet of clusters of ultra-fine solid particles that condensed from the vapor by collision with the cold ambient gas. The mean free path of Ar gas at 0.3 bar and 300 K is ∼300 nm. The ambient gas, being secondarily heated by the sample assembly, starts to make a convective motion and carries away the condensed particles. The convection continues until the laser power is shut off, and condensates remain suspended throughout the experiments. To collect the condensates, a valve to the vacuum pot is opened and the condensates are vacuum-suctioned onto a filter paper.

We apply two laser powers, 200 and 50 W, in expectation of some temperature effects on the chemical fractionations. Thus, we have four sets of combinations, viz., two initial compositions (L^{sil} and Allende) and two laser powers. For convenience, we distinguish four groups of experiments with IDs: L200 (L^{sil} and 200 W), L50, A200 (Allende and 200 W) and A50.

After each run, glass droplets are collected from the Cu-plates with a needle under a microscope. Glass droplets are also collected from the chamber wall with a brush. Most of the condensed particles are collected on a filter paper by vacuum suction; those attached to the Cu-plates and the chamber wall are also collected with a brush but not used for analysis.

Chemical analysis

A collection of the recovered glass droplets from each run was handled as follows. Because the number of droplets is different from run to run, <200-5000, we randomly picked 100-500 droplets from each collection, depending on the size of collection. The selected droplets for each run were then divided into five bins in accordance with their diameters, mounted on separate graphite discs (10 mm in diameter) with epoxy resin, polished down so as to expose cross-sections of all the mounted droplets, and carbon-coated. The condensed particles on a filter paper are easy to handle since they are compressed into a sheet-like layer, which is removed from the paper and mounted on a carbon conductive adhesive tape and carbon-coated on its surface.

Instrumental chemical analyses were made on those samples described above, with a FE-SEM-EDS (model JEOL JSM-7001F) at the Pheasant Memorial Laboratory for Geochemistry and Cosmochemistry, Institute for Study of the Earth's Interior, Misasa, Japan. The analytical conditions, 15 kV for accelerating voltage and 3 nA for probe current, were chosen for probing glassy and amorphous samples without evaporating volatile Na and K. The glass droplets were found to be uniform in composition; therefore, a single beam-rastering analysis over a large sample area was made on each droplet. The sheet

of condensed particles was relatively inhomogeneous, so that three beam-rastering analyses covering nearly an entire sheet area were applied.

Experimental results

Table 2 shows the experimental conditions and some results including maximum temperature recorded with pyrometer, and mass loss (%) relative to the initial mass, for four groups of experiments, discriminated with their IDs. The recorded T_{max} needs caution as indicated in "Experimental procedure" section and is explained in detail in "Time-temperature profiles" section. The mass loss (%) is calculated by a simple subtraction of the post weight of the assembly (sample + Re + graphite) from its initial weight; it includes weight losses not only of sample but also of Re wire and graphite disk. This is because the assembly parts are difficult to separate from one another after the experiments. In "Chemical evolution of MLB driven by evaporation" section, we adopt an alternative and unambiguous definition of 'vaporization degree'.

We have carried out many preliminary experiments (~150 runs) before the present work, using similar initial materials and methods. Droplets and condensates produced in these experiments were not chemically analyzed, but they back up the present work, especially in the temperature measurements. Instead of presenting the whole data of those experiments, we point out the use of preliminary data wherever necessary.

Characteristics of the droplets and the condensed particles

Figures 2 and 16 in Appendix A show video frames of the experiments. Bright and straight rays are the trajectories of silicate droplets that were ejected radially from the sample (Fig. 2a). Silicate vapor condenses immediately by colliding with a cold inert gas, making clusters of ultrafine particles that circulate in the convective motion of the gas inside the chamber (Fig. 2b).

The halos are the effect of light-scattering by the condensed particles, and obstruct the view of the laser-irradiated sample in the video images. Observation through a filtered-scope attached to the pyrometer revealed a restless and vibrating sample with many dotted lights and shades changing incessantly. They are vapor bubbles that grow and collapse on the sample surface ("Jet-droplets as origin of chondrules" section).

Figure 3a shows an example of silicate droplets quenched as glass, which were collected from inside the chamber. The smallest is several μm in diameter, while the largest is ~400 μm in diameter. Most droplets are in the range 10-100 μm. Figure 3b is a SEM image of the condensed particles. Individual particles are 50-100 nm in diameter and are connected 3-dimensionally to one another. They are probably amorphous judging from their round shapes.

Time-temperature profiles

As described in "Experimental procedure" section, the pyrometer scope was not always pointed at the hot spot of the charge. As a result, the T_{max} in Table 2 does not necessarily represent the true maximum temperature reached by the sample. This is particularly so in the 200 W experiments due to a short time for adjusting the scope position. In the 50 W experiments, however, it was mostly successful because more time was available to reposition the pyrometer.

Figure 4 shows a time-temperature profile of a successfully recorded run with a laser power of 200 W (run# 3 from preliminary experiments). The temperature reaches 2200 °C in one second, then it rises gradually to its maximum, ~2600 °C in 14 s. The inflection in temperature at ~2200 °C, referred to as T_B (and t_B for its time), is similar in all experiment groups, L200, L50, A200 and A50. For the 200 W experiments, the average (t_B, T_B) is (0.6 s, 2217 °C) from eight selected runs, and for 50 W it is (15 s, 2202 °C) from twenty-two selected runs.

The maximum temperature reached for each experiment group is obtained by averaging several highest T_{max} values in the same group of experiments, including the present and preliminary experiments. We selected runs# 138, 115, 60-2, and 36 for L200; runs# 91, 59 and 57 for A200; runs# 123, 121, 119, 118, 117, 113 and 24 for L50; and runs# 109 and 104 for A50. Their average T_{max} values are 2865 °C, 2673 °C, 2693 °C and 2576 °C, respectively, as shown in Table 3. These values would change a little by adding or subtracting runs in their selected lists, but their differences can be clearly indicated that T_{max} for 200 W is higher than for 50 W, and T_{max} for L^{sil} is higher than for Allende.

The recorded temperatures with pyrometer need corrections to account for absorption and scattering by the quartz window and the prism. The combined effective transmittance measured in advance was 95%. The pyrometer's output assumes a unit emissivity, viz., $\varepsilon = 1$, for any measured object, but emissivities of both L^{sil} and Allende are unknown. Table 3 shows T_{max} and T_B values for four experiment groups after corrections of the transmittance and four emissivity values (0.9, 0.8, 0.7 and 0.6).

T_B is most likely a boiling point at 0.3 bar, because it is constant regardless of the laser powers applied. (It also means that the boiling points of L^{sil} and Allende are similar). Silicate droplets were almost immediately (within a second) ejected from the samples when using a laser power of 200 W, while ejection began 10-20 s after the onset for 50 W. In "Jet-droplets as origin of chondrules" section, it is shown that those droplets are jet-droplets released by bursting of vapor bubbles during boiling.

The reason why the time-temperature derivative becomes small after T_B is reached is that the boiling regulates the sample temperature due to the large latent heat

Table 2 Experimental conditions and results

Run#	Initial Material	Laser Power (W)	Ambient Gas (bar)	T_{max} (°C)	Heating Duration (s)	Sample Shape	Holder System	Sample Initial Weight (g)	Mass Loss (wt%)	Recov. Drop.*1	Recov. Vap.*2
					Group ID: **L200**						
114	L^{sil}	200	$0.3Ar + 0.01H_2$	2603	14	m.c.	G+Re	0.01480	9.3	n	Y
115	L^{sil}	200	$0.3Ar + 0.01H_2$	2928	20	m.c.	G+Re	0.01407	?	Y	Y
126	L^{sil}	200	$0.3Ar + 0.01H_2$	1987	2	m.c.	G+Re	0.01520	13.7	Y	Y
127	L^{sil}	200	$0.3Ar + 0.01H_2$	2123	2	m.c.	G+Re	0.01510	27.3	Y	Y
128	L^{sil}	200	$0.3Ar + 0.01H_2$	1811	4	m.c.	G+Re	0.01481	4.0	Y	Y
129	L^{sil}	200	$0.3Ar + 0.01H_2$	2212	8	m.c.	G+Re	0.01489	48.0	Y	Y
130	L^{sil}	200	$0.3Ar + 0.01H_2$	1855	6	m.c.	G+Re	0.01493	29.2	Y	Y
131	L^{sil}	200	$0.3Ar + 0.01H_2$	2345	9	m.c.	G+Re	0.01454	81.8	Y	Y
132	L^{sil}	200	$0.3Ar + 0.01H_2$	2183	8	m.c.	G+Re	0.01497	97.4	Y	Y
133	L^{sil}	200	$0.3Ar + 0.01H_2$	2077	1	m.c.	G+Re	0.01460	77.7	Y	Y
137-1	L^{sil}	200	$0.3Ar + 0.01H_2$	1940	1	m.c.	G+Re	0.01437	4.5	Y	Y
137-2	re	200	$0.3Ar + 0.01H_2$	1870	2	r.r.	G+Re	—	5.6	Y	y
137-3	re	200	$0.3Ar + 0.01H_2$	1910	2	r.r.	G+Re	—	16.5	Y	y
137-4	re	200	$0.3Ar + 0.01H_2$	1608	2	r.r.	G+Re	—	1.5	n	y
137-5	re	200	$0.3Ar + 0.01H_2$	2182	5	r.r.	G+Re	—	22.6	Y	y
137-6	re	200	$0.3Ar + 0.01H_2$	1693	2	r.r.	G+Re	—	4.0	Y	y
138	L^{sil}	200	0.3Ar	2799	24	m.c.	G+Re	0.01501	104.0	Y	Y
					Group ID: **L50**						
113	L^{sil}	50	$0.3Ar + 0.01H_2$	2672	245	m.c.	G+Re	0.01498	>100	Y	Y
117	L^{sil}	50	$0.3Ar + 0.01H_2$	2613	31	m.c.	G+Re	0.01508	32.7	Y	Y
118	L^{sil}	50	$0.3Ar + 0.01H_2$	2776	61	m.c.	G+Re	0.01499	47.2	Y	Y
119	L^{sil}	50	$0.3Ar + 0.01H_2$	2702	87	m.c.	G+Re	0.01485	49.8	Y	Y
120	L^{sil}	50	$0.3Ar + 0.01H_2$	2450	128	m.c.	G+Re	0.01443	81.6	Y	Y
121	L^{sil}	50	$0.3Ar + 0.01H_2$	2733	132	m.c.	G+Re	0.01490	94.5	Y	Y
122	L^{sil}	50	$0.3Ar + 0.01H_2$	2387	81	m.c.	G+Re	0.01379	35.1	Y	Y
123	L^{sil}	50	$0.3Ar + 0.01H_2$	2695	140	m.c.	G+Re	0.01481	41.9	Y	Y
124	L^{sil}	50	$0.3Ar + 0.01H_2$	2298	464	m.c.	G+Re	0.01507	60.3	n	Y
125-1	L^{sil}	50	$0.3Ar + 0.01H_2$	1600	17	m.c.	G+Re	0.01468	3.5	n	Y
125-2	re	50	$0.3Ar + 0.01H_2$	1617	16	r.r.	G+Re	—	3.6	n	y
125-3	re	50	$0.3Ar + 0.01H_2$	1723	16	r.r.	G+Re	—	9.7	n	y
125-4	re	50	$0.3Ar + 0.01H_2$	1450	17	r.r.	G+Re	—	17.3	n	y
125-5	re	50	$0.3Ar + 0.01H_2$	2123	17	r.r.	G+Re	—	2.0	n	y
134	L^{sil}	50	$0.3Ar + 0.01H_2$	1770	22	m.c.	G+Re	0.01488	2.4	n	Y
135	L^{sil}	50	$0.3Ar + 0.01H_2$	1484	2	m.c.	G+Re	0.01500	1.3	n	Y
136	L^{sil}	50	$0.3Ar + 0.01H_2$	1505	19	m.c.	G+Re	0.01415	10.9	n	Y
					Group ID: **A200**						
91	Allende	200	$0.3Ar + 0.01H_2$	2608	8	m.c.	G+Re	0.01437	117.0	Y	Y
93-1	Allende	200	$0.3Ar + 0.01H_2$	1010	4	m.c.	G+Re	0.01500	6.5	Y	Y
93-2	re	200	$0.3Ar + 0.01H_2$	2084	3	r.r.	G+Re	—	17.2	Y	Y
93-3	re	200	$0.3Ar + 0.01H_2$	1532	3	r.r.	G+Re	—	52.4	Y	Y
93-4	re	200	$0.3Ar + 0.01H_2$	2189	2	r.r.	G+Re	—	24.9	Y	Y

Table 2 Experimental conditions and results (*Continued*)

Run#	Initial Material	Laser Power (W)	Ambient Gas (bar)	T_{max} (°C)	Heating Duration (s)	Sample Shape	Holder System	Sample Initial Weight (g)	Mass Loss (wt%)	Recov. Drop.*1	Recov. Vap.*2
93-5	re	200	$0.3Ar + 0.01H_2$	2372	1	r.r.	G+Re	—	30.2	Y	Y
93-6	re	200	$0.3Ar + 0.01H_2$	2215	2	r.r.	G+Re	—	6.9	Y	Y
93-7	re	200	$0.3Ar + 0.01H_2$	2139	9	r.r.	G+Re	—	7.2	Y	Y
94	Allende	200	$0.3Ar + 0.01H_2$	902	2	m.c.	G+Re	0.01491	44.0	Y	Y
95	Allende	200	$0.3Ar + 0.01H_2$	2280	2	m.c.	G+Re	0.01482	?	n	Y
96	Allende	200	$0.3Ar + 0.01H_2$	2187	3	m.c.	G+Re	0.01467	61.0	Y	Y
97	Allende	200	$0.3Ar + 0.01H_2$	2052	4	m.c.	G+Re	0.01446	46.0	Y	Y
98	Allende	200	$0.3Ar + 0.01H_2$	2148	2	m.c.	G+Re	0.01443	45.0	Y	Y
99	Allende	200	$0.3Ar + 0.01H_2$	1701	10	m.c.	G+Re	0.01446	61.0	Y	Y
100	Allende	200	$0.3Ar + 0.01H_2$	2031	12	m.c.	G+Re	0.01477	59.0	Y	Y
101	Allende	200	$0.3Ar + 0.01H_2$	2122	14	m.c.	G+Re	0.01397	104.0	Y	Y
112	Allende	200	$0.3Ar + 0.01H_2$	2495	6	m.c.	G+Re	0.01491	>100	Y	Y
					Group ID: **A50**						
90	Allende	50	$0.3Ar + 0.01H_2$	2313	218	m.c.	G+Re	0.01428	97.0	Y	Y
102-1	Allende	50	$0.3Ar + 0.01H_2$	1436	3	m.c.	G+Re	0.01469	3.4	n	Y
102-2	re	50	$0.3Ar + 0.01H_2$	1723	27	r.r.	G+Re	—	8.9	n	y
102-3	re	50	$0.3Ar + 0.01H_2$	1471	13	r.r.	G+Re	—	23.3	n	y
102-4	re	50	$0.3Ar + 0.01H_2$	1075	7	r.r.	G+Re	—	10.5	n	y
102-5	re	50	$0.3Ar + 0.01H_2$	806	6	r.r.	G+Re	—	3.1	n	y
102-6	re	50	$0.3Ar + 0.01H_2$	1329	7	r.r.	G+Re	—	2.2	n	y
102-7	re	50	$0.3Ar + 0.01H_2$	1391	13	r.r.	G+Re	—	7.7	n	y
102-8	re	50	$0.3Ar + 0.01H_2$	809	13	r.r.	G+Re	—	7.9	n	y
102-9	re	50	$0.3Ar + 0.01H_2$	1195	34	r.r.	G+Re	—	16.3	n	y
102-10	re	50	$0.3Ar + 0.01H_2$	2258	112	r.r.	G+Re	—	14.4	y	y
103	Allende	50	$0.3Ar + 0.01H_2$	2177	34	m.c.	G+Re	0.01429	23.1	Y	Y
104	Allende	50	$0.3Ar + 0.01H_2$	2591	186	m.c.	G+Re	0.01474	45.0	Y	Y
105	Allende	50	$0.3Ar + 0.01H_2$	1855	26	m.c.	G+Re	0.01395	24.9	Y	Y
106	Allende	50	$0.3Ar + 0.01H_2$	2364	85	m.c.	G+Re	0.01423	38.3	Y	Y
107	Allende	50	$0.3Ar + 0.01H_2$	2472	188	m.c.	G+Re	0.01456	42.7	Y	Y
108	Allende	50	$0.3Ar + 0.01H_2$	2469	230	m.c.	G+Re	0.01470	46.4	Y	Y
109	Allende	50	$0.3Ar + 0.01H_2$	2559	417	m.c.	G+Re	0.01419	53.1	Y	Y
110	Allende	50	$0.3Ar + 0.01H_2$	2420	749	m.c.	G+Re	0.01426	70.2	Y	Y
111	Allende	50	$0.3Ar + 0.01H_2$	2288	598	m.c.	G+Re	0.01462	90.8	Y	Y

Note. ∗1: Recovery of droplets. ∗2: Recovery of vapor. Allende: Allende meteorite.
L^{sil}: synthetic L silicate. re: residue of the preceding run. m.c.: miniature cylinder.
r.r.: rounded residue. G+Re: Graphite disk and rhenium wire. Y: recovered and analyzed.
y: recovered but not analyzed. n: not recovered. T_{max}: lower limits for T_{max} (see the text)

of vaporization. The steady increase in temperature afterwards may result from two effects: the evaporation rate, hence latent heat loss rate, becomes gradually smaller due to the selective loss of volatiles with time, and the radiative loss of energy becomes smaller due to gradual shrinkage of the sample by evaporation. The latent heat control also explains why the difference in T_{max} between L200 and L50, or between A200 and A50, is only 100-200 °C, while the laser power differs by a factor of four. The lower T_{max} for Allende as compared to L^{sil} is explained by a higher concentration of FeO, which is more volatile than MgO, in the former.

Accepting T_B as the boiling point at 0.3 bar, T_B ~2300 °C (which corresponds to $\varepsilon = 0.9$ in Table 3) is too low for boiling (Hashimoto 1983). Therefore, $\varepsilon \leq 0.8$ should be more realistic.

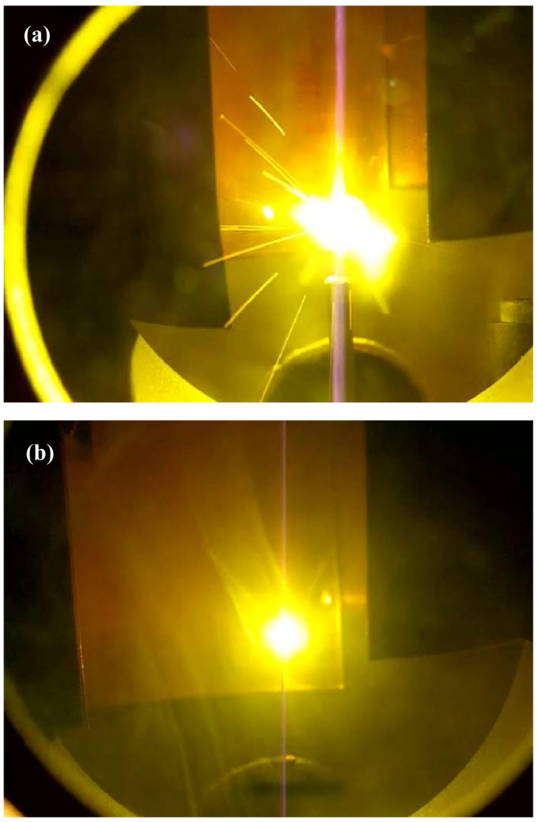

Fig. 2 Video frames (30 frames s^{-1} and 1/60 s for exposure) of the scenes in the experiments for **a** run# 84 and **b** run# 32. The molten sample (MLB) sits in the center of the bright halo, and the laser beam comes from the 10 o'clock direction. **a** A dozen droplets, seen as bright and straight rays, are radially ejected from the MLB almost simultaneously. (One droplet is actually seen at the tip of the ray in the 10 o'clock position). **b** A smoke composed of condensed particles rises from the evaporating MLB, while clusters of previously condensed particles form sheet-like structures in the convective motions of the ambient gas. This scene was taken within a fraction of second after the laser power was shut off, when the MLB temperature dropped below the boiling point

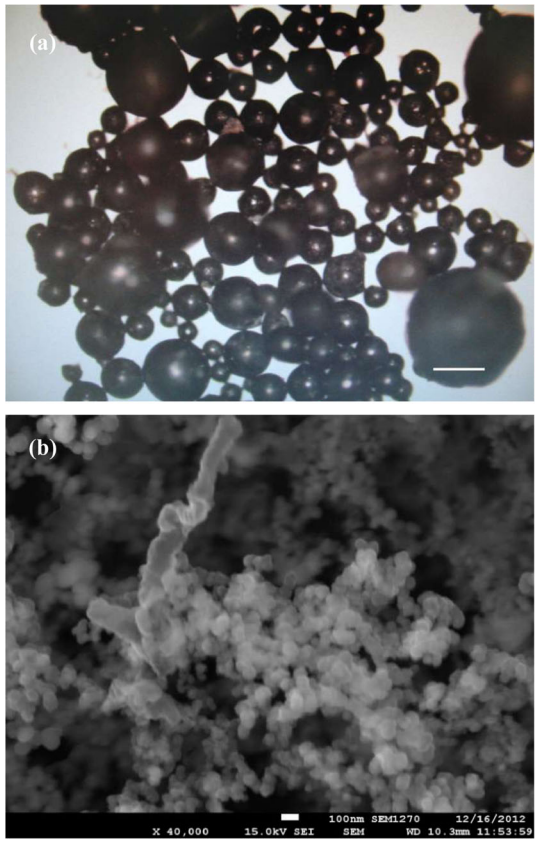

Fig. 3 a Glass-quenched droplets collected from inside the chamber. Scale bar = 100 μm. They are generally spherical in shape, with a flat face on one side that results from collision with a Cu-plate or the chamber wall. Necking between the spherules is an optical artifact. **b** SEM image of the condensed particles collected on a filter paper. Scale bar = 100 nm. Globules of 100 nm or less in diameter are 3-dimensionally connected to one another

Size-frequency distribution of silicate droplets

We collected all droplets (677 in total) in run# SZ6 (run conditions similar to L200) and nearly all droplets in run# 138 to determine the size-frequency distribution of the ejected droplets. All droplets were measured for their diameters under a microscope. In run# SZ6, their range in diameter is 9-390 μm, and were sorted into size bins of every 5 μm width for a normal-scale histogram (Fig. 5a). The same droplets were size-sorted into common log-scale bins of every 0.065 width (Fig. 5b). The result is a log-normal-like distribution, which is generally recognized as a typical size-frequency distribution of chondrules (Friedrich et al. 2015). In a similar manner, the size-frequency distribution of the droplets in run# 138 (3067 droplets) was obtained, which also resembles a log-normal distribution.

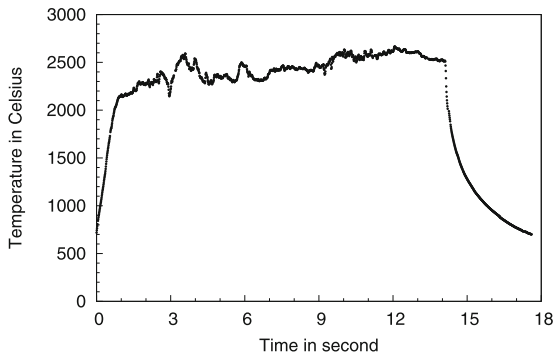

Fig. 4 Time-temperature profile of the MLB surface in run# 3 (200 W). The temperature is recorded automatically once it exceeds 700 °C. The laser power was shut off after 14 s, at which point radiative cooling started

Table 3 Measured and corrected temperatures of MLB surface

ID	Meas (ε=1)		tm 0.95, ε 0.9		tm 0.95, ε 0.8		tm 0.95, ε 0.7		tm 0.95, ε 0.6	
	T_B	T_{max}	T_B	T_{max}	T_B	T_{max}	T_B	T_{max}	T_B	T_{max}
L200	2217	2865	2317	2991	2395	3088	2488	3206	2597	3343
A200	2217	2673	2317	2792	2395	2883	2488	2994	2597	3123
L50	2202	2693	2302	2812	2379	2904	2472	3016	2580	3146
A50	2202	2576	2302	2690	2379	2778	2472	2886	2580	3011

Note. Temperature is shown in °C. Meas: Measured temperature.
tm: Transmittance. ε: Emissivity. See text for T_B and T_{max}

The total mass of ejected droplets are calculated from their size and frequency, assuming a complete sphere and density of 3 g cm^{-1}. The mass of ejection thus obtained is divided by the total mass lost by the sample to give a mass fraction of droplets to the total mass loss. The mass fractions for runs# SZ6 and 138 are 11.9 and 11.0%, respectively.

Chemical evolution of MLB driven by evaporation

The silicate droplets are sprayed pieces of the boiling MLB. Therefore, their chemical compositions represent that of the MLB at the time of their ejection. Since the droplets are ejected all the time as long as boiling continues, they are good tracers of any compositional changes in the MLB that is driven by continuous evaporation.

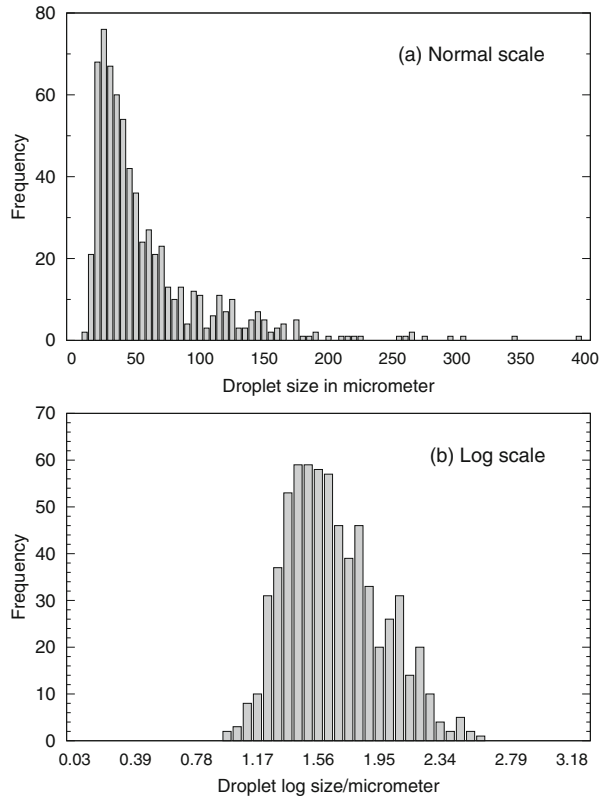

Fig. 5 Size-frequency distribution of silicate droplets recovered from run# SZ6. **a** Normal scale. **b** Common logarithmic scale

The relative timing of ejection of a particular droplet can be known from the Al concentration in the droplet, for the reasons described below. An aluminum oxide ($AlO_{1.5}$) is one of the super-refractory oxides amongst the constituents of the chondritic meteorites. It is by far the most refractory of the ten elements (in their oxide forms) included in the present experiments, and does not evaporate until the other nine elements have completely vaporized (Hashimoto et al. 1979; Hashimoto 1983). The unchanging mass of Al in the MLBs guarantees the following relationship, as long as mass loss is caused solely by evaporation.

$$MX_{Al} = M'X'_{A1}. \quad (1)$$

Here M is a total number of moles of the ten elements in the MLB, and X_{Al} is a molar fraction of Al in the MLB; superscript ($'$) denotes post-evaporation and no superscript pre-evaporation.

We define the vaporization degree (VD) of the MLB as follows,

$$VD(\%) = 100\left(\frac{M_0 - M'}{M_0}\right) = 100\left(1 - \frac{X_{Al,0}}{X'_{Al}}\right). \quad (2)$$

Here M_0 denotes the initial total number of moles in the MLB, and $X_{\mathrm{Al},0}$ denotes the initial mole fraction of Al in the MLB. Because each silicate droplet is a piece of the MLB, it registers its moment of ejection as MLB's VD% and also represents the chemical composition of the MLB at that moment.

Figure 6 shows the concentrations of the nine elements in the ejected droplets as functions of their Al concentrations for the L200 experiment group (856 droplets altogether for chemical analyses) and for the A200 experiment group (851 droplets). The Al concentration increases from its initial value 2.88 mol% for L^{sil} and 3.40 mol% for Allende to the highest 39.42 mol% for L200 and 71.46 mol% for A200, corresponding to a VD range from 0 to 92.7% for L200 and from 0 to 95.2% for A200. The highest Al mol% (or VD%) might be larger since not all droplets from the same group of experiments are used for chemical analyses. The results for the groups, L50 and A50 show trends that are similar to L200 and A200, respectively.

We may divide the ten elements into five groups according to their difference in evaporative fractionation. 1) Alkaline elements, Na and K, are very volatile and distill out of MLB in a very early phase of evaporation. In the

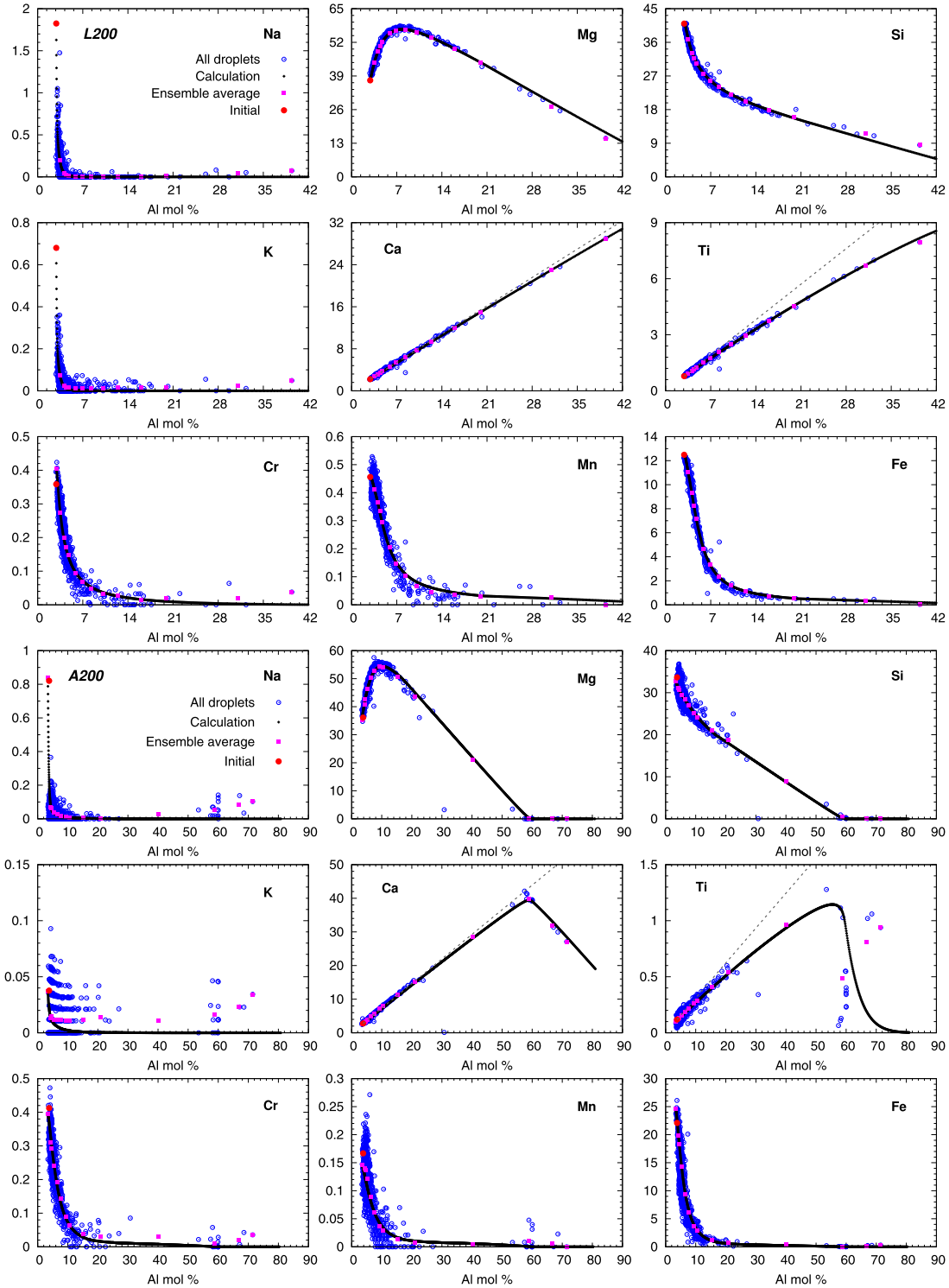

Fig. 6 Element concentration in mol% in the droplets as a function of Al mol% for the experiment groups L200 and A200. 'All droplets' indicate all of the droplets analyzed for each group. The 'Initial' composition is either L^{sil} for L200 or Allende for A200. For 'Ensemble average', refer to "Derivation of relative volatilities from the experimental results" section and Table 4. 'Calculation' denotes the calculated composition of the MLB that evolves by evaporation, starting with the initial composition, either of L^{sil} or of Allende. See "Application of relative volatilities to an arbitrary MLB: self-consistency test" section for detail. The dotted lines in the Ca and Ti panels indicate extension of the lines that connect the origin and their initial concentration

present experiments, 80-90% of these elements were lost by the time boiling started. 2) Si, Fe, Cr and Mn are moderately volatile and their concentrations in the MLB steadily decrease as VD increases. 3) Mg is more refractory than the second group of elements. Thus, at first it increases in concentration in the MLB as the second group are preferentially lost, but soon comes its turn for depletion. 4) Ca and Ti are more refractory than Mg, and become steadily enriched in the MLB up until Al reaches ~60 mol% (or VD ~95%), when they start to decrease in concentration (as is seen in A200). 5) Al is more refractory than Ca and Ti, and does not evaporate before Ca and Ti distill out.

Relative volatilities of the ten elements

Definition of relative volatility and mathematical method of its derivation

Hashimoto (1983) defined 'volatility' (ζ) of an oxide component in a silicate liquid to quantify its ease for escape to vacuum.

$$\zeta_i = \frac{J_i}{C_i}, \tag{3}$$

where J_i is the vacuum evaporation rate of component i per unit area and unit time (mole cm^{-2} s^{-1}) at a given temperature, and C_i is its molar concentration (mole cm^{-3}) in the silicate liquid. Generally, evaporation rate is proportional to the concentration of the component. Hence, volatility is expected to be roughly constant. He applied it to the three components, SiO_2, MgO and FeO in the five component silicate liquid, and found that their volatilities are nearly constant for a wide range of their concentrations at a constant temperature.

We propose that the relative magnitudes in volatilities of the oxide components are enough to predict the chemical fractionations caused by evaporation, and extend this idea by introducing 'relative volatility' of j-th to i-th component in the liquid,

$$Z_{j/i} = \frac{\zeta_j}{\zeta_i}. \tag{4}$$

Unlike volatilities, the relative volatilities are insensitive to temperature variations as long as the volatilities of the j-th and i-th components vary proportional to the inverse temperature with similar slopes. We take advantage of this quality in the analyses to follow, i.e., data analyses from "Derivation of relative volatilities from the experimental results" section to "Application of relative volatilities to an arbitrary MLB: self-consistency test" section, and also model analyses in fitting chondrule chemistry in "Model calculation of chondrule chemistry" section.

We consider an infinitesimal evaporation of a multicomponent silicate liquid which include oxide components i and j as well as Al-oxide ($AlO_{1.5}$), for an infinitesimal time dt. Then the mass of evaporation of the i-th component (in moles) in dt is,

$$dm_i = J_i A dt. \tag{5}$$

Here A is the surface area of the silicate liquid. C_i is written using the molar volume of the liquid (V_M) and the molar fraction of i (X_i) in the liquid,

$$C_i = \frac{X_i}{V_M}. \tag{6}$$

Substitution of Eqs. 3 and 6 into Eq. 5 makes

$$dm_i = \frac{\zeta_i X_i A dt}{V_M}. \tag{7}$$

Hence it follows

$$\frac{dm_j}{dm_i} = \frac{\zeta_j}{\zeta_i}\frac{X_j}{X_i}. \tag{8}$$

Considering the Al-oxide as a non-evaporating substance as explained in "Chemical evolution of MLB driven by evaporation" section and using Eq. 1, dm_i is expressed as

$$\begin{aligned} dm_i &= m_i - m_i' \\ &= MX_i - M'X_i' \\ &= M\frac{X_i X_{Al}' - X_i' X_{Al}}{X_{Al}'}. \end{aligned} \tag{9}$$

Here again, superscript ($'$) denotes post-evaporation and no superscript pre-evaporation. Hence it follows

$$\frac{dm_j}{dm_i} = \frac{X_j X_{Al}' - X_j' X_{Al}}{X_i X_{Al}' - X_i' X_{Al}}. \tag{10}$$

Finally, substituting $X_{\mathrm{Al}}'/X_{\mathrm{Al}}$ by q and equating Eq. 8 with Eq. 10,

$$\frac{\zeta_j}{\zeta_i} = \frac{qX_j - X_j'}{qX_i - X_i'}\frac{X_i}{X_j}. \tag{11}$$

Thus, relative volatility is a function of molar fractions only. We take SiO_2 for the i-th component unless otherwise noted.

If evaporation is not infinitesimal, the term X_i/X_j in Eq. 11 should be replaced with $(X_i + X_i')/(X_j + X_j')$, and the obtained relative volatility is an average value.

Derivation of relative volatilities from the experimental results

We obtain relative volatilities for the ten oxide components for the two groups, L200 and A200, from the chemical compositions of the ejected droplets. Theoretically speaking, a set of two droplet compositions with different VD values is enough to calculate relative volatilities for all elements relative to Si by using Eq. 11. The actual compositional data, however, indicate that the droplet compositions do not define smooth functions of VD or Al mol%, but more or less scatter about the general trends. Since (relative) volatility is basically a differential quantity, it is sensitive to data scattering. There is a means to get

away from this difficulty, but beforehand let us specify a possible cause for the scattering of the data.

Although analytical errors contribute to data dispersion, it is not considered as the main cause because of the relatively high precision of the chemical analyses. We found that the FeO contents in the droplets are too variable from one droplet to another even if their Al mol% or VD are nearly identical. This was more prominent for A200 droplets than L200 droplets. We identified that chemical reactions of the MLB with the sample holder, either the graphite disk or Re-wire, caused FeO to be partially reduced into metal, leaving the MLB depleted in FeO in places where the liquid silicate was in direct contact with those holder materials. Allende contains twice as much FeO as that of L^{sil} in its initial composition, making it very susceptible to the reduction reactions. If local heterogeneity in FeO content is not effectively averaged out by diffusion (slow) and stirring (fast) driven by boiling, it will persist. Silicate droplets were ejected from many places in the MLB and should sample local heterogeneity in FeO concentration. The FeO heterogeneity extends its effect to other oxide components in MLB because the chemical composition is always normalized to 100%.

We took 856 droplets from the L200 experiments (851 droplets from A200), arranged them in the increasing order of the Al content, and divided them into thirteen ensembles in the following manner. Since droplets with low Al concentrations are large in number, the sizes of ensembles (viz., the number of droplets in them) are configured so that each ensemble is spaced as equally as possible in terms of its average Al concentration. In addition, to obtain a smooth change in chemical composition, each ensemble overlaps its quarter or half of constituent droplets with the preceding as well as following ensemble (a method of ensemble moving average). The average chemical compositions of thirteen ensembles for L200 are shown in Table 4 and Fig. 6 (upper nine panels). Those for A200 are shown in Table 4 and Fig. 6 (lower nine panels).

The lower sections in Table 4 show relative volatilities of the ten elements calculated with Eq. 11 from adjacent pairs of ensemble averages of their concentrations. Note that the term X_i/X_j is replaced with $(X_i + X_i')/(X_j + X_j')$ in Eq. 11, because it is a finite evaporation that proceeded between successive ensembles.

Relative volatilities of Mg and Fe

Table 4 shows that the relative volatility of Mg to Si ($Z_{Mg/Si}$) increases as VD or Al mol% increases. This apparent trend is not related to Al, but $Z_{Mg/Si}$ is clearly related to the Mg/Si ratio as indicated by their linear relationship in Fig. 7a. In liquid silicates, the type and concentration of network-modifying cations that coordinate to the anionic SiO_4 tetrahedra dictate their physical and thermodynamic properties (Toop and Somis 1962; Yokokawa and Niwa 1969; Masson 1972; Hess 1977; Richet and Bottinga 1986; Stebbins et al. 1995). Comparing Fe and Mg, Mg is a stronger base and selectively coordinates to SiO_4 (Yokokawa and Niwa 1969), making Mg more refractory than Fe. As the Mg concentration in the liquid increases, however, the bond energy per Mg atom to the SiO_4 tetrahedron should be reduced, thus making it less refractory. Si should act in opposite way: with more Mg the total bond energy per SiO_4 should become larger, making it more refractory as the Mg concentration increases. This explains why the relative volatility of Mg increases with increasing Mg/Si ratio.

The relative volatility of Mg for A200 is systematically higher than for L200. This may be explained by either (1) the effect of FeO concentration, or (2) the effect of temperature. Allende has twice as much FeO compared to L^{sil}. Although the basicity of Fe is far smaller than that of Mg (Yokokawa and Niwa 1969), its overabundance would have an obstructing effect on Mg in monopolizing SiO_4 tetrahedra. However, the difference in relative volatility in Fig. 7a does not reduce even if the FeO concentration in MLB decreases to a level of 5 mol% for A200. So this effect alone is not enough. Hashimoto (1983) indicated that the volatility of MgO is relatively increased at lower temperatures compared to that of SiO_2. As shown in "Time-temperature profiles" section, the recorded T_{max} for A200 experiments is lower than for L200 by 200 K. The temperature effect, however, explains only 12% increase in relative volatility. Therefore, we presume both effects work together.

$Z_{Mg/Si}$ rises abruptly at high Mg/Si ratios, 2.7 for L200 and 2.3 for A200. The sudden increases are caused by the high concentration of Ca in the MLB (Hashimoto 1983) because Ca is a stronger network-modifier than Mg (Yokokawa and Niwa 1969). As long as Ca concentration is low, its impeding effect on Mg is limited. As evaporation proceeds, however, Ca is steadily increased in expense of more volatile elements. When Ca/Si ratio exceeds 0.6, where more than halves of SiO_4 tetrahedra are preferentially coordinated to Ca, Mg cations start to be freed from bondage with the SiO_4 tetrahedra. Therefore, it is the effect not of high Mg/Si ratio but of concentrated Ca that raises $Z_{Mg/Si}$ higher than unity.

Figure 7b shows a linear anti-correlation between $Z_{Mg/Si}$ and $Z_{Fe/Mg}$ that obtain by dividing $Z_{Fe/Si}$ with $Z_{Mg/Si}$, for both L200 and A200. This anti-correlation may be explained by the competitive relationship between Mg and Fe in coordinating to SiO_4 tetrahedra. The linearity fails at the highest values of $Z_{Mg/Si}$ for both L200 and A200; this is again explained as the effect of high Ca concentration. The failure at the low end for L200 can be explained by a large structural change in the silicate liquid which should happen when Mg/Si ratio crosses 1. The data point of L200 with the lowest $Z_{Mg/Si}$, viz., 0.09, corresponds to the

Table 4 Average chemical compositions of 13 ensembles (upper sections) and relative volatilities of elements (lower sections)

L200		Ensemble Average, mol% (Total =100)											
E#	data#	Na	Mg	Al	Si	K	Ca	Ti	Cr	Mn	Fe	Mg/Si	Ca/Si
0	initial	1.824	37.285	2.882	40.982	0.680	2.220	0.783	0.405	0.456	12.484	0.910	0.054
1	1-400	0.198	44.121	3.506	36.707	0.075	2.718	0.935	0.274	0.411	11.053	1.202	0.074
2	301-600	0.041	48.552	4.083	33.189	0.023	3.157	1.079	0.198	0.366	9.311	1.463	0.095
3	401-700	0.022	50.559	4.415	31.655	0.016	3.421	1.162	0.170	0.334	8.246	1.597	0.108
4	501-750	0.015	52.274	4.787	30.341	0.014	3.731	1.261	0.148	0.296	7.132	1.723	0.123
5	650-800	0.006	55.383	5.904	27.578	0.012	4.619	1.533	0.095	0.206	4.665	2.008	0.167
6	716-815	0.004	56.593	6.911	25.797	0.011	5.360	1.763	0.068	0.148	3.344	2.194	0.208
7	751-830	0.003	56.680	8.308	24.019	0.011	6.400	2.075	0.047	0.103	2.352	2.360	0.266
8	781-840	0.003	55.867	10.149	22.013	0.013	7.738	2.475	0.032	0.066	1.643	2.538	0.352
9	801-850	0.003	53.838	12.400	20.161	0.015	9.386	2.966	0.026	0.046	1.159	2.670	0.466
10	826-853	0.005	49.513	15.991	17.908	0.015	12.046	3.744	0.015	0.037	0.726	2.765	0.673
11	840-855	0.011	44.022	19.967	15.906	0.017	14.901	4.548	0.019	0.029	0.579	2.768	0.937
12	852-856	0.048	27.239	31.031	11.619	0.023	22.929	6.708	0.020	0.028	0.354	2.344	1.973
13	856	0.073	14.920	39.418	8.515	0.049	28.994	7.953	0.038	0.000	0.040	1.752	3.405
		ζ_j/ζ_i (i = Si)										pair average	
E-pair	ζ_{Fe}/ζ_{Mg}	Na	Mg	Al	Si	K	Ca	Ti	Cr	Mn	Fe	Mg/Si	Ca/Si
0-1	11.487	5.899	0.090	0.000	1.000	5.878	(0.021)	0.060	1.908	0.977	1.038	1.048	0.064
1-2	5.728	5.789	0.223	0.000	1.000	4.828	0.010	0.038	1.860	1.059	1.279	1.326	0.084
2-3	5.310	5.564	0.300	0.000	1.000	3.467	(0.018)	0.030	1.840	1.358	1.591	1.528	0.101
3-4	4.745	3.446	0.386	0.000	1.000	1.552	(0.046)	(0.007)	1.797	1.637	1.831	1.659	0.115
4-5	4.149	3.772	0.497	0.000	1.000	1.354	(0.012)	0.046	2.120	1.866	2.061	1.859	0.144
5-6	3.593	2.148	0.605	0.000	1.000	0.826	0.038	0.079	2.191	2.173	2.175	2.098	0.187
6-7	2.922	1.282	0.714	0.000	1.000	0.690	0.026	0.082	2.153	2.108	2.086	2.274	0.236
7-8	2.593	1.423	0.746	0.000	1.000	0.159	0.036	0.083	2.009	2.206	1.935	2.445	0.307
8-9	2.301	0.753	0.823	0.000	1.000	0.377	0.025	0.067	1.412	1.966	1.894	2.601	0.406
9-10	2.116	(0.689)	0.907	0.000	1.000	0.650	0.013	0.056	2.095	1.298	1.918	2.715	0.563
10-11	1.318	(1.818)	0.997	0.000	1.000	0.285	0.027	0.080	(0.039)	1.290	1.314	2.766	0.797
11-12	1.013	(1.072)	1.214	0.000	1.000	0.150	0.013	0.067	0.509	0.658	1.230	2.589	1.374
12-13	2.222	(0.332)	1.505	0.000	1.000	(0.877)	0.008	0.125	(0.671)	4.096	3.345	2.094	2.579
A200		Ensemble Average, mol% (Total =100)											
E#	data#	Na	Mg	Al	Si	K	Ca	Ti	Cr	Mn	Fe	Mg/Si	Ca/Si
0	initial	0.8366	35.193	3.400	32.822	0.0367	2.467	0.100	0.394	0.146	24.605	1.072	0.075
1	31～200	0.0665	40.933	4.246	31.179	0.0131	3.181	0.122	0.310	0.140	19.808	1.313	0.102
2	101～300	0.0631	42.495	4.521	30.676	0.0145	3.399	0.130	0.292	0.137	18.272	1.385	0.111
3	301～650	0.0397	46.381	5.317	29.493	0.0119	3.996	0.154	0.241	0.121	14.245	1.573	0.135
4	501～730	0.0268	50.342	6.420	28.500	0.0115	4.815	0.184	0.191	0.089	9.419	1.766	0.169
5	601～770	0.0174	52.943	7.639	27.070	0.0115	5.736	0.216	0.142	0.061	6.164	1.956	0.212
6	681～805	0.0110	54.362	9.385	25.084	0.0107	7.088	0.263	0.090	0.037	3.669	2.167	0.283
7	721～815	0.0094	54.199	10.486	24.166	0.0108	7.909	0.287	0.065	0.029	2.839	2.243	0.327
8	801～830	0.0047	50.518	15.290	21.132	0.0115	11.414	0.407	0.038	0.014	1.171	2.391	0.540
9	825～834	0.0032	43.665	20.977	18.846	0.0138	15.236	0.539	0.031	0.007	0.681	2.317	0.808
10	834～835	0.0263	20.926	40.211	8.816	0.0107	28.658	0.960	0.031	0.004	0.358	2.374	3.251

Table 4 Average chemical compositions of 13 ensembles (upper sections) and relative volatilities of elements (lower sections) (*Continued*)

11	835∼848	0.0537	0.268	58.864	0.465	0.0166	39.792	0.482	0.010	0.010	0.038	0.576	85.57
12	848∼851	0.0816	0.013	66.787	0.061	0.0229	31.995	0.813	0.021	0.006	0.199	0.218	527.9
13	851	0.1029	0.000	71.460	0.036	0.0344	27.090	0.938	0.035	0.000	0.302	0.000	752.3
		ζ_j/ζ_i (i = Si)										pair average	
E-pair	ζ_{Fe}/ζ_{Mg}	Na	Mg	Al	Si	K	Ca	Ti	Cr	Mn	Fe	Mg/Si	Ca/Si
0-1	6.200	7.066	0.259	0.000	1.000	4.279	(0.116)	0.065	1.683	0.966	1.604	1.189	0.088
1-2	5.666	1.448	0.320	0.000	1.000	(0.439)	(0.046)	0.005	1.582	1.087	1.815	1.349	0.106
2-3	5.512	3.076	0.369	0.000	1.000	1.769	0.002	(0.043)	1.755	1.399	2.036	1.477	0.123
3-4	5.616	2.585	0.477	0.000	1.000	1.013	0.010	0.042	1.885	2.217	2.681	1.668	0.152
4-5	4.808	2.659	0.547	0.000	1.000	0.770	(0.006)	0.059	2.072	2.455	2.630	1.859	0.190
5-6	3.987	2.337	0.635	0.000	1.000	0.998	(0.020)	0.037	2.329	2.451	2.533	2.057	0.246
6-7	3.213	1.774	0.769	0.000	1.000	0.685	0.009	0.161	2.933	2.489	2.470	2.204	0.304
7-8	2.720	2.054	0.874	0.000	1.000	0.595	0.020	0.053	1.774	2.071	2.378	2.312	0.427
8-9	1.835	1.661	1.073	0.000	1.000	0.318	0.063	0.083	1.174	2.327	1.968	2.356	0.667
9-10	0.939	(0.697)	0.984	0.000	1.000	0.653	0.013	0.050	0.479	0.883	0.924	2.335	1.587
10-11	0.858	(0.141)	1.069	0.000	1.000	(0.027)	0.024	0.477	0.630	(0.236)	0.917	2.284	7.376
11-12	(0.638)	(0.172)	1.164	0.000	1.000	(0.117)	0.206	(0.231)	(0.342)	0.412	(0.743)	0.535	136.6
12-13	(0.167)	(0.283)	3.585	0.000	1.000	(0.575)	0.405	(0.131)	(0.749)	3.585	(0.599)	0.137	611.5

Note. E# denotes ensemble number. E-pair denotes ensemble pair. 'Mg/Si' and 'Ca/Si' denote molar ratios of elements in each ensemble. 'pair average' is average of ensemble pair. Subscript *j* denotes elements. Bracketed values denote negative values

ensemble pair 0-1 in Table 4, which encompasses Mg/Si ratio from 0.9 to 1.2. A200, on the other hand, does not cross 1 in Mg/Si because the initial Mg/Si for Allende is 1.072.

The systematic shift in $Z_{Fe/Mg}$ of A200 from L200 in Fig. 7b may be a temperature effect. According to Hashimoto (1983), the volatility of FeO is relatively increased at lower temperatures compared to that of MgO. A temperature difference of 200 K in the temperature range near 3000 K changes $Z_{Fe/Mg}$ by a factor of 1.3, explaining the offset of A200 from L200.

Relative volatilities of other elements

The relative volatility of Cr, $Z_{Cr/Si}$, for L200 is nearly constant from ensemble pair 0-1 through 9-10, and its average is 1.94. For A200, $Z_{Cr/Si}$ correlates well with and is roughly proportional to $Z_{Fe/Si}$ with a proportionality factor of 0.9. $Z_{Mn/Si}$ is roughly proportional to $Z_{Fe/Si}$ with a proportionality factor of 0.9 for L200 and 0.8 for A200.

The values of $Z_{Na/Si}$ and $Z_{K/Si}$ for L200 are valid only for the ensemble pairs 0-1, 1-2, 2-3 and 3-4 for Na, and 0-1 and 1-2 for K. This is because the Na concentration beyond ensemble 4 and the K concentration beyond ensemble 2 are below their detection limits (0.01 mol% for Na; 0.02 mol% for K) in chemical analyses. Hence the average of four ensemble pairs for Na and that of two pairs for K give 5.2 for $Z_{Na/Si}$ and 5.4 for $Z_{K/Si}$, respectively. These values may, however, represent their relative volatilities only appropriate to low concentrations in Na and K. The shortcoming comes from the way of organizing the ensembles in "Derivation of relative volatilities from the experimental results" section, where moderately volatile elements are optimized so as to derive their relative volatilities over concentration ranges. Very volatile Na and K evaporate in the earliest phase and their concentration decrease quickly down to their detection limits.

To try to overcome these shortcomings, we have arranged another set of thirteen ensembles, using the same 856 droplets data, which allocates more numbers of ensembles for the early phase of evaporation. The derived average values for $Z_{Na/Si}$ and $Z_{K/Si}$ are 5.41 from six ensemble pairs (1-2, 2-3, 3-4, 4-5, 5-6 and 6-7) and 5.05 from four pairs (1-2, 2-3, 3-4 and 4-5), respectively. They are the values to be used in the following sections.

The first pair 0-1 of the new set, viz., the tie between the initial composition and the earliest sixty droplets, however, reveals $Z_{Na/Si}$ and $Z_{K/Si}$ to be ∼10, much larger than the other pairs. If the number of the earliest droplets is reduced to as small as five, the pair 0-1 reveals $Z_{Na/Si}$ and $Z_{K/Si}$ to be ∼30. This means that Na and K at the earliest evaporation phase of MLB are much more volatile, relative to Si, than in later phases. This is explained as a temperature effect because highly volatile elements such as Na and K have considerably smaller heats of vaporization compared to that

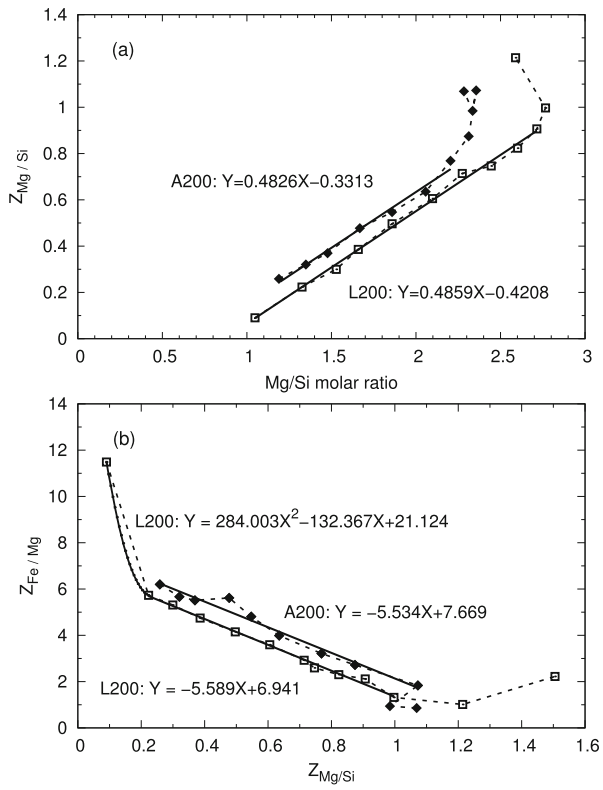

Fig. 7 a $Z_{Mg/Si}$ as a function of the Mg/Si molar ratio for L200 and A200. **b** $Z_{Fe/Mg}$ as a function of $Z_{Mg/Si}$ for L200 and A200. Each data point represents an ensemble pair in Table 4. Linear or quadratic regressions to the data are shown as solid lines, with their equations. X: abscissa. Y: ordinate

of SiO_2. As described in "Time-temperature profiles" section, it took the MLB ~0.5 s to reach its boiling point, by which time significant amounts of Na and K have already evaporated at relatively low temperatures. The first few droplets must have stemmed from MLB just when it reached a full boiling point.

The $Z_{Na/Si}$ derived for A200 gives lower values than for L200, 2.42 on average of five ensemble pairs. The first pair gives ~7 for $Z_{Na/Si}$, again much larger than the other pairs. A further analysis has indicated that $Z_{Na/Si}$ is ~10 at the earliest evaporation phase. The initial concentration of K in Allende is already too close to its detection limit, making it impossible to derive a reliable $Z_{K/Si}$.

Ca and Ti are too refractory to evaporate until late stages, making it difficult to accurately determine their relative volatilities for early ensemble pairs. Late ensemble pairs are too rich in Ca (viz., Ca/Si >0.6) and Al, representing Ca, Al-rich liquids rather than a silicate liquid. From these considerations, the ensemble pair 9-10 for L200 is only suitable for determination of $Z_{Ca/Si}$ and $Z_{Ti/Si}$ for a chondritic silicate liquid. We adopt 0.01 for $Z_{Ca/Si}$ and 0.06 for $Z_{Ti/Si}$ for L200. For A200, the ensemble pair 7-8 is suitable, and we adopt 0.02 for $Z_{Ca/Si}$ and 0.05 for $Z_{Ti/Si}$. Al does not evaporate or is assumed not to, hence $Z_{Al/Si} = 0$. By definition $Z_{Si/Si} = 1$.

Application of relative volatilities to an arbitrary MLB: self-consistency test

Introduction of the new quantitative measure, relative volatility, has made clear the following important facts. 1) The Mg/Si ratio in MLB is a dominant factor that determines volatilities of the major elements, Mg, Si and Fe as well as Mn. The result is quite essential in evaluating evaporative fractionation of chondritic materials and also of planetary materials, which are basically Mg, Fe-rich silicate bodies. 2) The relative volatilities of all elements estimated here are similar both for L200 and for A200, implying that the relative volatilities are insensitive to the initial composition of the MLB. This fact provides support for our attempt to predict the evaporative fractionation trends of silicate liquids having arbitrary compositions.

We wish to predict evaporative fractionation of a silicate liquid having an arbitrary initial composition by adopting the relative volatility: $Z_{j/i}$ (i = SiO_2). We assume that a silicate MLB is composed of oxides of the ten elements, Na, Mg, Al, Si, K, Ca, Ti, Cr, Mn and Fe, and is homogeneous in composition throughout evaporation. After infinitesimal evaporation of the MLB, the molar fraction of j-th oxide is written by using Eqs. 4 and 11,

$$X'_j = qX_j - Z_{j/i}X_j(q - \frac{X'_i}{X_i}). \tag{12}$$

Here $q = X'_{Al}/X_{Al}$. Replacing j with a dummy k and summing both sides of Eq. 12 for all ten oxides,

$$\sum_k X'_k = q\sum_k X_k - (q - \frac{X'_i}{X_i})\sum_k (Z_{k/i}X_k). \tag{13}$$

Appreciating that the sum of molar fractions of all oxides is unity,

$$1 = q - (q - \frac{X'_i}{X_i})\sum_k (Z_{k/i}X_k). \tag{14}$$

Replacing the term $\sum_k (Z_{k/i}X_k)$ with b, it follows

$$X'_i = X_i\frac{(bq - q + 1)}{b}. \tag{15}$$

Accordingly, X'_i, the molar fraction of i-th oxide in the MLB after infinitesimal evaporation is obtained from its previous value X_i. By inserting X'_i into Eq. 12, X'_j for all other oxides are calculated. With q taken to be close to unity (e.g., 1.005), Eqs. 12 and 15 are iteratively solved to give a set of X_i and X_j for any given Al mol% or VD% of MLB starting from an arbitrary initial set of X_i and X_j.

Expressing the composition of the vapor with molar fractions Y_l ($l = i$ or j), the vapor composition at every iteration step (Y_l^{dif}, called differential vapor composition) is given by

$$Y_l^{dif} = \frac{X_l - \frac{X'_l}{q}}{\sum_k (X_k - \frac{X'_k}{q})}. \quad (16)$$

Here k takes all ten oxides. The composition of the total vapor accumulated in N iterations from the start, $Y_{l,N}^{int}$ or the integrated vapor composition, is given by summing the differential vapor over all of the iteration steps,

$$Y_{l,N}^{int} = \frac{\sum_N Y_{l,n}^{dif}}{\sum_k \sum_N Y_{k,n}^{dif}}. \quad (17)$$

Here $Y_{l,n}^{dif}$ and $Y_{k,n}^{dif}$ are the differential vapor compositions at iteration step# n.

In the above derivation, we have not included a possible contribution of the ejection of jet-droplets during the course of evaporative fractionation of MLB. Even if the jet-droplet mass is taken into account, the chemical compositions of the MLB and the differential vapor are not affected and are given by Eqs. 12, 15 and 16, since only the mass of the MLB is reduced. The integrated vapor composition, however, is affected and Eq. 17 is replaced by,

$$Y_{l,N}^{int} = \frac{\sum_N \left\{ \prod_n (1 - \varepsilon_n) \right\} Y_{l,n}^{dif}}{\sum_k \sum_N \left\{ \prod_n (1 - \varepsilon_n) \right\} Y_{k,n}^{dif}}. \quad (18)$$

Here ε_n is the mass proportion of jet-droplets ejected at step# n, relative to the mass of the MLB at step# n. In the case where the ejected mass as jet-droplets is negligibly small, Eq. 17 is strictly valid.

We have applied Eqs. 12, 15, 16 and 17 to the initial MLB compositions of L^{sil} and Allende, to check for self-consistency of the set of relative volatilities determined for all ten elements, and whether they reproduce the chemical composition of the MLB (viz., droplets) and vapor (viz., condensates) obtained in the experiments. The set of relative volatilities and their applicable conditions are summarized in Table 5. The iteration was executed with a constant q (either 1.005 or 1.002, depending on a required precision) from VD = 0 to 95%. The result is shown in Figs. 6 (upper nine panels) for L200. As shown in Fig. 6, the calculation reproduces the composition trajectories of the MLB defined by droplets quite well. Figure 8 compares the calculated trajectories of the integrated vapor with the bulk compositions of condensed particles in the experiments. Although the bulk condensates (experiments) scatter in composition due to their own heterogeneity ("Chemical analysis" section), their general trends are reproduced by the calculated trajectories rather well. The convincing result in the self-consistency test justifies both the L200 experiment and the use of relative volatilities derived from it. It also indicates that the effect of mass loss by ejection of jet-droplets on the composition of the integrated vapor is small, since the total mass loss in our experiments as jet-droplets was less than ~10% of the initial mass of the MLBs.

The same calculations were made for A200. The set of relative volatilities for A200 used is shown in Table 5. The compositional trajectories of the MLB defined by the droplets are well reproduced by the calculation, as shown in Fig. 6 (lower nine panels). As shown in Fig. 8 (lower six panels), however, the integrated vapor does not follow the general trends of the bulk condensates, except for Na. The Fe content in the bulk condensates is systematically low as compared to that of the calculated vapor, being explained by the loss of FeO from the MLB as a result of reduction reactions that proceeded in the Allende experiments ("Derivation of relative volatilities from the experimental results" section). Its effect is two fold: 1) the MLB and droplets from it become depleted in FeO, indicating superficially a high evaporation rate of FeO and hence its large relative volatility that is used in the calculation; 2) the condensates from the vapor are depleted in FeO, indicating superficially its low evaporation rate in the experiment. The high Si (and Mg) content in the bulk condensate, as compared to that in the calculated integrated vapor, is considered a compensating effect of the Fe depletion as a result of normalization to 100 mol%. It should not largely affect minor elements such as Mn and Cr, but they also considerably deviate from the calculated trajectories. As a result, the discrepancies in composition between the experimental condensates and the calculated integrated vapor disqualifies A200 for further use of its derived relative volatilities.

Discussion

It is required for a proper model of chondrule formation that the 3.5 fundamental features of chondrules must be explained. 1) Why is their maximum size 1-5 mm? In addition, why do they distribute in log-normal-like size distribution? 2) Why are their chemical compositions so variable? 3) Why are their petrographic textures variable? We attempt to answer all these questions in the following discussion.

First we identify the silicate droplets in our experiments as splash droplets that eject from collapsing cavities of vapor bubbles, known as 'jet-droplets' in the field of atmospheric and oceanic science. If jet-droplets are origin of chondrules, the characteristic size of bubbles, approximately ten times the size of the droplets, requires a dense and large silicate body as a chondrule source, named 'duston'. Accordingly it is postulated that chondrules are jet-droplets from large boiling silicate bodies ("Jet-droplets as origin of chondrules" section).

A boiling duston should accompany a large vapor cloud expanding adiabatically, where jet-droplets must

Table 5 The estimated relative volatilities and their applicable conditions

Conditions	$Z_{Mg/Si}$
L200	
C < 1 and X < 1.052	0.093
C < 1 and 1.052 < X < 2.924	$0.4859X - 0.4208$
C < 1 and X > 2.924	1
C > 1	1
A200	
C < 0.6 and X < 0.8937	0.1
C < 0.6 and 0.8937 < X < 2.758	$0.4826X - 0.3313$
C < 0.6 and X > 2.758	1
C > 0.6	1

Conditions	$Z_{Fe/Mg}$
L200	
C < 1 and Y < 0.2232	$284.003Y^2 - 132.367Y + 21.124$
C < 1 and 0.2232 < Y < 1.0631	$-5.589Y + 6.941$
C < 1 and Y > 1.0631	1
C > 1	1
A200	
C < 0.667 and Y < 1.205	$-5.534Y + 7.669$
C < 0.667 and Y > 1.205	1
0.667 < C < 1.587	$-0.9733C + 2.4834$
C > 1.587	0.9242

Conditions	$Z_{Na/Si}$	$Z_{K/Si}$	$Z_{Ca/Si}$	$Z_{Ti/Si}$	$Z_{Cr/Si}$	$Z_{Mn/Si}$	$Z_{Fe/Si}$
L200							
$VD < 8.5\%$	$f(VD)$	$f(VD)$	0.01	0.06	1.94	$0.9Z_{Fe/Si}$	$Z_{Fe/Mg} \times Z_{Mg/Si}$
$VD > 8.5\%$	5.41	5.05	0.01	0.06	1.94	$0.9Z_{Fe/Si}$	$Z_{Fe/Mg} \times Z_{Mg/Si}$
A200							
$VD < 9\%$	$f_1(VD)$	$f_2(VD)$	0.02	0.05	$0.9Z_{Fe/Si}$	$0.8Z_{Fe/Si}$	$Z_{Fe/Mg} \times Z_{Mg/Si}$
$VD > 9\%$	2.42	2.42	0.02	0.05	$0.9Z_{Fe/Si}$	$0.8Z_{Fe/Si}$	$Z_{Fe/Mg} \times Z_{Mg/Si}$

Note. C: Ca/Si molar ratio. X: Mg/Si molar ratio. Y: $Z_{Mg/Si}$.
$f(VD) = 0.2854(VD)^2 - 5.194VD + 29.27$.
$f_1(VD) = -0.8867VD + 10.35$.
$f_2(VD) = -0.2568VD + 5.09$

react with vapor and with condensed dust, thereby re-accommodate volatiles lost during evaporation. This mechanism should produce a wide spectrum in chondrule chemistry. A model calculation with use of experimentally obtained relative volatilities demonstrates that various chondrule compositions are nearly completely reproduced from the initial CI composition by considering the vaporization degree and redox state of Fe ("Origin of chondrule chemistry" section). The model also naturally explains other features of chondrules ("Origin of other features of chondrules" section).

A possible mechanism required for heating dustons must be energetic enough to cause their surface to boil. We will explore such a heat source in the companion paper (II). Here we take it as a prerequisite because boiling is a key to the formation of chondrules in our model.

The main bodies of dustons with their surfaces heat-scorched, are decoupled from chondrules and fine dust due to the aerodynamic effect, and are assembled into planetesimals by their self-gravities. The fate of dustons as well as chondrite-forming materials after the chondrule formation will be explored in detail in the companion paper (II).

Jet-droplets as origin of chondrules

Evidence for the ejected droplets being jet-droplets

We first point out preceding works on ejection of droplets from bursting air bubbles on the surfaces of fresh and sea

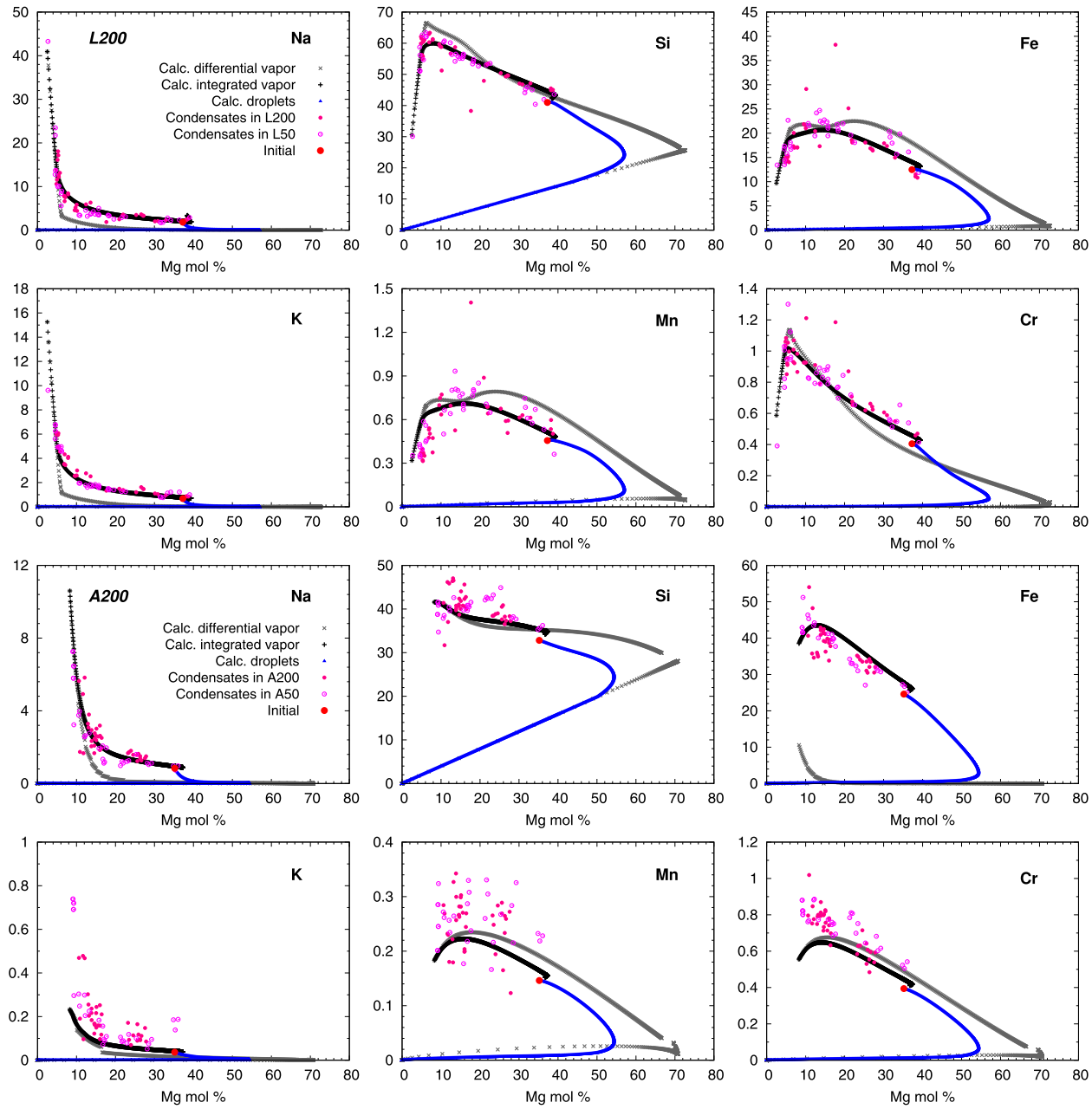

Fig. 8 Numerical reproduction of evaporation and condensation trajectories for the experiment groups L200 and A200. Element concentration in mol% is shown in each panel as a function of Mg mol%. 'Calc. droplets', 'Calc. differential vapor' and 'Calc. integrated vapor' are numerical results (see "Application of relative volatilities to an arbitrary MLB: self-consistency test" section). 'Condensates in L200' are the bulk compositions of the condensed particles in the experiments that belong to L200, and are compared to 'Calc. integrated vapor'. The L50 data are added for reinforcement since they exhibit similar trends to the L200 data. The same approach was applied when plotting and modeling the A200 data. The 'Initial' composition is either L^{sil} for L200 or Allende for A200

water (e.g., Kientzler et al. 1954; Hayami and Toba 1958; Blanchard 1989). Two distinct mechanisms, jet-droplets and film-droplets, have been studied as a possible major source of sea-salt aerosols in terrestrial atmosphere (e.g., O'Dowd et al. 1997). (Some details of these mechanisms are described in Appendix A).

Jet-droplets are produced in a series of steps (Georgescu et al. 2002): a bubble bursts on a liquid surface; the gaping bubble cavity collapses; a surface capillary wave converges axially, generating an upward high-speed liquid jet; and a successive fragmentation of the jet produces one to several jet-droplets. These are visually shown in successive

frames in Fig. 14d in Appendix A (MacIntyre 1972). One noticeable characteristics of jet-droplets is their vertical ejection from a bulk liquid surface. In our experiments silicate droplets are ejected radially from the spherical MLB surface (Figs. 2a and 16 in Appendix A), indicating that their ejection angle is normal to the spherical surface.

Other features of jet-droplets known from the freshwater and seawater experiments can be compared with our experiments. Spile (1994, 1995, 1997), in his high-speed camera analyses, observed 1-6 droplets in each bubble burst event, with ejection speeds of 0.1-10 m s^{-1}. In our experiments, 1-3 droplets were observed per bubble burst, with velocities of 0.3-4 m s^{-1} (see Fig. 16 in Appendix A). Our measurements, however, were biased by the limitations of the available video images: the viewing area of ~90 mm across and the shutter speed 30 frames s^{-1} meant that the maximum number and velocity of droplets were limited to 3 and 4 m s^{-1}, respectively.

In the water jet-droplet experiments, the size ratio of jet-droplet to its original air bubble is known to be 1/10-1/5. In our preliminary experiment (run# V2; see Fig. 15 in Appendix A), which used a high-speed video camera, the size ratio of droplet/bubble was observed to be ~1/6.

There is another line of evidence for jet-droplets, which used CO bubbles in iron liquid and N_2 bubbles in liquid mercury (Distin et al. 1968). Figure 3 in their paper shows that a single bubble burst produced more than three iron droplets, and it is also calculated from the figure that the droplet/bubble size ratio was ~1/10 and that the droplets were ejected at 4 m s^{-1}. The size ratio of mercury droplet/bubble is estimated 1/11-1/7 from their description (Distin et al. 1968).

Admittedly, our experiments lack high-speed images of the moment of ejection of jet-droplets, but all lines of evidence acquired so far indicate that jet-droplet phenomena are common to any kind of liquid with any kind of bubble gas in it.

Evidence for chondrules being jet-droplets

If jet-droplets are the origin of chondrules, the maximum size of chondrules, 1-5 mm depending on chemical types of chondrites, must be explained by the maximum size possible for jet-droplets. Our experiments produced a droplet with the largest diameter ~0.4 mm, while the diameter of the MLB at its earliest stage before significant evaporation was 2.1 mm. Distin et al. (1968) observed the largest iron droplet ~1 mm in diameter, while the diameter of molten iron body (2 g) is calculated to be 8.2 mm. King (1982, 1983) reported a ~0.7 mm silicate drop (in King 1982, figure 8), while the initial diameter of molten bulk Allende sample (~2 g) was ~10 mm. All three experiments indicate that the maximum droplet sizes observed in them are 1/5-1/15 times those of the MLBs. This fact implies that their observed maximum droplet sizes are controlled by the maximum possible bubble sizes, or strictly saying the maximum cavity diameters after they burst, which should be no larger than the sizes of MLBs. This may lead to a tentative suggestion that the maximum chondrule diameter was determined by the size of their precursory melt body and is 1/10-1/5 of the latter.

Yet another plausible constraint as to the maximum chondrule size comes from the study of water jet-droplets. It is known that there are upper size limits for bubbles that can produce jet-droplets upon bursting at the surface of water and other solvents (Resch and Afeti 1991a; Suzuki and Mitachi 1995; Georgescu et al. 2002). For a distilled water, the upper size limit is 5.4 mm in diameter (Suzuki and Mitachi 1995).

According to Blantachette and Bigioni (2006) the capillary wave must travel a quarter of the circumference along the cavity surface from edge to bottom before being damped by viscous dissipation (Fig. 14d in Appendix A). It travels at the wave velocity given by $v_w = (\sigma k/\rho)^{1/2}$ (Landau and Lifshitz 1987) and reaches the bottom in time $t = (\pi R_b/2)/(\sigma k/\rho)^{1/2}$, where R_b is radius of the cavity, σ surface tension, k wave number, ρ density of the liquid. The attenuation efficiency f is given by $f = 2\mu k^2/\rho$ (Landau and Lifshitz 1987), where μ is dynamic viscosity. The condition for the wave to reach the bottom without its complete dissipation is $ft < 1$. Thus the critical bubble radius for ejection of jet-droplet is given by

$$R_{cr} = \frac{1}{\mu}\left(\frac{1}{\pi k^{3/2}}\right)(\rho\sigma)^{1/2}. \tag{19}$$

Georgescu et al. (2002) obtained numerically critical bubble radii for twenty kinds of liquids (Table 7 in Appendix B), including freshwater and seawater, in good agreement with experimentally determined critical bubble radii. We have calculated wave numbers k for the twenty solvents using Eq. 19 and the values for R_{cr}, ρ, σ and μ given by Georgescu et al. (2002), and found that there is a good linear correlation between log μ and log k as shown in Fig. 17 in Appendix B. Using Eq. 25, we can calculate wave numbers for various silicate liquids from their known dynamic viscosity, and apply its result to obtain their critical bubble radii using Eq. 19.

Table 6 shows R_{cr} for peridotite, dunite and enstatite compositions at 2400, 2700 and 3000 °C. The surface tension was assumed constant, 0.4 N m^{-1}, for all temperatures since its temperature dependence is small. We

Table 6 Critical bubble radius

T	R_{cr} (m)		
(°C)	Peridotite	Dunite	Enstatite
3000	0.01275	0.01329	0.01036
2700	0.01196	0.01248	0.00971
2400	0.01104	0.01154	0.00901

have used data by Bottinga and Weill (1972) for viscosity and data by Nelson and Carmichael (1979) for densities, and extrapolated those to high temperatures. Chondritic composition is more or less close to dunite among the three compositions. Accordingly $2R_{cr}$, viz., the maximum bubble diameter for jet-droplet ejection, is 23-27 mm for 2400-3000 °C, and the corresponding jet-droplet size is 4.6-5.4 mm in diameter by assuming the 1/5 size ratio of droplet to bubble (the size ratio slightly increases with bubble size). This size range of jet-droplets is very similar to the maximum chondrule size of ordinary chondrites, hence explains the upper limit of the chondrule size as well as the lower abundances for larger chondrules. An use of non-Arrhenian T-dependence of viscosity (e.g., Giordano et al. 2008) in the calculation, instead of the Bottinga and Weill (1972) data extraporated to higher temperatures, reduces R_{cr} by only 10%. Thus, this conclusion does not change.

The maximum chondrule sizes for carbonaceous chondrites are generally smaller than those for ordinary chondrites (Friedrich et al. 2015). It could be explained if the boiling temperatures of dustons were below 2400 °C because (1) the higher viscosity for lower-temperature liquids should dampen the capillary wave more effectively, (2) smaller bubbles obey the ∼1/10 rule for the jet-droplet/bubble size ratio, rather than 1/5 for large bubbles, and (3) carbonaceous chondrites, hence their precursors should contain more volatiles (e.g., H_2O and organic compounds), that would lower their boiling temperatures.

If the size of a MLB is larger than the R_{cr} of bubbles, R_{cr} determines the chondrule maximum size; if a MLB is smaller than R_{cr}, the size of the MLB determines the upper limit for chondrule size. For ordinary chondrites whose maximum chondrule diameter ranges in 2-6 mm (Friedrich et al. 2015) it is required that their MLBs must be larger than 10-30 mm in diameter. For other types of chondrites whose chondrule sizes tend to be smaller than those in ordinary chondrites, the sizes of their MLBs could be smaller than 10-30 mm. This, however, is not decisive because the lower-temperature boiling could also explain their smaller size ranges. It is also plausible that only limited areas of their MLBs were heated above their boiling point; in that case jet-droplets were ejected from bubbles much smaller than the MLB size.

Another feature that characterizes chondrules is their size range and size-frequency distribution. The size-frequency distributions of chondrules have been measured for nearly all types of chondrites. Most data, however, are biased because the chondrule size is usually determined on polished sections of meteorites, which means that a measured size is nothing but a cross-sectional diameter. Statistically hundreds or thousands of measurements on a single chondrite would produce a size-frequency distribution somewhat similar to its real distribution, but it tends to be shifted towards smaller sizes and also creates an artifact in that there is no cut-off for the smallest size. The measurements using the disaggregation method is only trusted, in which statistically meaningful analyses (e.g., at least two hundreds measurement for each chondrite) show log-normal-like size-frequency distributions with a size range (maximum/minimum size ratio) of 10-15 (Friedrich et al. 2015).

As shown in "Size-frequency distribution of silicate droplets" section, the size-frequency distribution of jet-droplets in two experimental runs exhibited log-normal-like distributions. This makes a strong argument that jet-droplets from bursting bubbles are origin of chondrules.

In his solar-furnace evaporation experiments using the Murchison meteorite, King (1982) observed droplet ejections similar to our experiments. Although he described them as a sputtering product, we suppose that they were jet-droplets judging from their size distribution shown in Rosin's size-frequency diagram. King (1982) is the first who proposed that no particular size sorting mechanism (e.g., Liffman and Brown 1995) is necessary after chondrule formation to explain their log-normal distribution.

Because of the straightforward size relationship between the jet-droplet and its natal bubble, it appears that the size-frequency distribution of bubbles must obey a log-normal size distribution. We presume that the product of the bubble size frequency and its bursting probability determines the size-frequency distribution of jet-droplets.

Duston as a source of chondrules

If chondrules were jet-droplets ejected from a molten silicate body, there should have existed a solid precursory body before its melting. The body is presumed to be composed of primordial dust in PPD, that is dense enough for holding a molten surface layer and larger than 20 mm in diameter from the consideration made in previous sections. We name such a body 'duston[1]' in order to distinguish it from the conventional image of fluffy dust-balls.

The collisional dust growth has been studied experimentally and its size limit known as a bouncing barrier has been suggested, several mm in its final diameter (e.g., Blum and Wurm 2008). However, the dust-collision experiments were performed mostly using aggregates of monomer grains (usually amorphous silica) with a single grain size, ∼1 μm. Ingredient particles of primordial dust, as inferred from interstellar dust, are extremely variable in their physical and chemical properties, including their

[1] 'Duston' is defined as a dense and large body (>20 mm in diameter) consisting of primordial dust in PPD, that is postulated to have existed as a source of chondrules. This new term is a hybrid of English and Japanese in a shortened form of dust-ton, which means a large, rounded unified mass of dust. As an example 'Futon', a Japanese mattress, is a combination of 'fu' and 'ton', which meant historically a large, round bundle (ton) of clothes (fu) to sit on.

grain sizes (e.g., Kim et al. 1994; Draine 2003; Natta et al. 2007; Waters 2015). The behavior of dust aggregates in collision: either stick, bounce, fragment or erode is hard to predict if various materials and their combinations with various grain sizes, especially in nanometer ranges, are involved (Blum 2018). Therefore, we still do not know if there is a barrier for the dust growth and how large the size limit would be if there was a barrier.

The existence of large dust aggregates is suggested from theoretical studies of giant planet formation, which have shown that pebble-sized materials are a key to the fast growth of giant planetary cores (Lambrechts and Johansen 2014; Levison et al. 2015). In-situ observations of the comet 67P/Churyumov-Gerasimenko in Rosetta mission revealed a very wide range in size of dust aggregates, from 10^{-5} to 10 meters (e.g., Fulle et al. 2016; Poulet et al. 2016; Ott et al. 2017; Pajola et al. 2017; Blum et al. 2017). The size range differs depending on the various dust-sensitive instruments onboard Rosetta and Philae, but it appears that most of the mass resides in the forms of decimeter particles (Blum et al. 2017). Blum et al. (2017) concluded that 67P/Churyumov-Gerasimenko likely formed through a gentle gravitational collapse of a bound clump of several-mm-sized pebbles, intermixed with microscopic ice particles. Recently, a multiwavelength analysis of (sub-)mm and cm continuum interferometric observations of three PPDs has shown that the maximum dust grain size decreases with distance from the central star and it tends towards similar values ∼2 cm in the innermost spatially resolved region 10 au < R < 20 au (Tazzari et al. 2016).

We suggest that the grain growth of primordial dust inevitably led to the formation of dustons, and that dustons dominated the dust mass function by the time chondrules started to form.

Origin of chondrule chemistry

Vapor cloud model

A boiling duston, as proposed here for the formation of chondrules, should be accompanied by a high density silicate vapor cloud around it. In a thin gas environment such as PPD, the vapor cloud would expand adiabatically with a subsonic velocity and subsequently cool to a supersaturated state. Jet-droplets, on the other hand, rapidly cool by radiative emission and possibly fall into a supercooled state. Naturally, they would condense vapor molecules upon collision en-route to the outside of the cloud and also incorporate the homogeneously-nucleated silicate dust at the vapor cloud-disk gas boundary. Toward a quantitative estimate of such processes, we first consider a simple steady state of the vapor cloud.

Figure 9 depicts a steady state vapor cloud with a boiling duston (surface temperature ∼3000 K) of radius r_0 in the center. We assume that an adiabatically expanding vapor

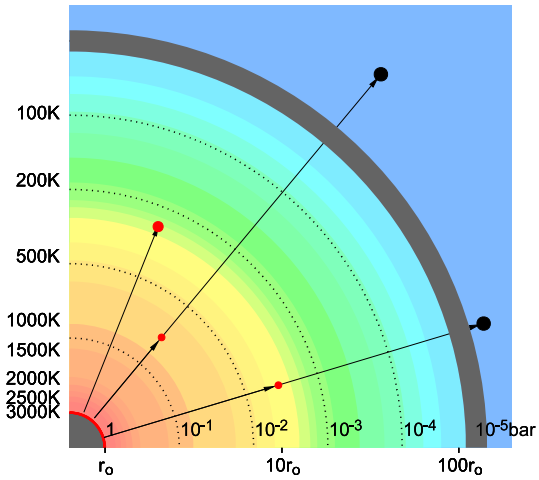

Fig. 9 Schematic diagram of a steady-state vapor cloud with a boiling duston surface ($r = r_0$) at constant T_0 = 3000 K and P_0 = 1 bar. Adiabatic expansion of the vapor cloud ends at $r \sim 100r_0$, where its pressure becomes equivalent to that of the disk gas (assumed 10^{-5} bar) and a whole condensation occurs as shown in gray belt. The abscissa is in log scale except $r < r_0$. Jet-droplets, shown in filled circle, eject from the duston surface and may grow in size by recondensation of the vapor and by incorporation of condensed particles on their way out

condenses as its pressure becomes equivalent to that of the surrounding disk gas (taken as 10^{-5} bar in Fig. 9), for two reasons. (1) Condensation of vapor needs a large heat sink for its latent heat to be absorbed, which the disk gas should provide. (2) Without preexisting solid nuclei, vapor must condense homogeneously. Homogeneously condensed particles in general are extremely fine-grained, typically one to tens of nm (e.g., Kato 1976; Rietmeijer et al. 1999, 2002, 2009). Particles much smaller than 1 μm cannot radiate at infrared wavelengths, thus cannot cool effectively. Even if they condensed, they should immediately reevaporate due to the latent heat deposited on them.

Nucleation and condensation of the vapor may happen well inside the vapor cloud, at least partially, if the maximum supersaturation at which a significant number of condensation nuclei form is reached before the vapor is depressurized to 10^{-5} bar. The maximum supersaturation, in turn, is determined by the interplay between two opposite influences: cooling of the vapor due to the work of expansion, and heating of the vapor due to the latent heat liberated during condensation (Raizer 1960). Here, a detailed examination on the nucleation is difficult and out of scope. However, even if the homogeneous nucleation occurred before the vapor was depressurized to 10^{-5} bar, the condensed particles would be accumulated near the boundary with the disk gas, because they should keep the same momentum as they had in the vapor state before condensation.

For simplicity, we choose the situation where the vapor homogeneously condenses as it reaches the boundary. Then, due to condensation, the silicate vapor pressure at the boundary becomes negligible, which ensures a free expansion of the following vapor that is continuously produced by the boiling duston. Hence, a steady state pressure profile is established throughout the cloud in less than 0.1 s for dustons smaller than 1 m. The vapor flux from the duston surface (as denoted by subscript '0') is equal to the flux passing through a sphere of arbitrary radius (as denoted by subscript '1').

$$4\pi r_0^2 \left(\frac{1}{4}\right) n_0 \bar{c}_0 = 4\pi r_1^2 \left(\frac{1}{4}\right) n_1 \bar{c}_1. \tag{20}$$

Here $\bar{c} = (8RT/\pi M)^{1/2}$ is the mean thermal velocity, r: radius, n: vapor density (mole m^{-3}), R: gas constant, T: absolute temperature, and M: the mean molecular weight of the vapor. A free expansion (into a vacuum space) proceeds adiabatically, hence from Eq. 20

$$\frac{P_1}{P_0} = \left(\frac{r_1}{r_0}\right)^{\frac{-4\gamma}{\gamma+1}}; \quad \frac{T_1}{T_0} = \left(\frac{r_1}{r_0}\right)^{\frac{4(\gamma-1)}{\gamma+1}}. \tag{21}$$

Here γ is the adiabatic index, and P_0 is the vapor pressure of silicate liquid at the duston surface T_0. Substituting γ = 1.6 for the silicate vapor and P_0 = 1 bar at 3000 K for a ~CI-chondritic composition, estimated from the data of Hashimoto (1983), the pressure and temperature profiles are given as functions of normalized radius, r_1/r_0, as shown in Fig. 9.

Now we turn to the jet-droplets that are ejected from the boiling duston. They travel through the vapor cloud in radial direction. We first make the simplest assumption that the jet-droplets do not interact with vapor at all, but that they cool independently by their own radiation and evaporation. The radiation from the duston's surface is also considered. Then the droplet's temperature T is given by

$$\frac{-4\pi a^3 \rho c_p}{3} dT = 4\pi a^2 Q(T) dt;$$
$$Q(T) = \sigma T^4 - \frac{1}{4}\sigma T_0^4 \left(\frac{r_o}{r}\right)^2 + \frac{\Delta h_v^o P_e}{\sqrt{2\pi MRT}}. \tag{22}$$

Here a: radius of the droplet (which is assumed constant because it changes little), ρ: its density (assumed constant), c_p: its specific heat (assumed constant), Δh_v^o: its latent heat of vaporization (assumed constant), T: its temperature (assumed uniform from surface to inside), P_e: its vapor pressure, M: mean molecular weight of the vapor (assumed constant), R: gas constant, and σ: Stefan-Boltzmann constant.

Integration of Eq. 22 and consideration of travel time $t = (r - r_0)/V_e$ (V_e: ejection speed) give

$$\int_{T_0}^{T} Q^{-1}(T) dT = -\left(\frac{3}{\rho c_p}\right)\left(\frac{r_0}{aV_e}\right)\left(\frac{r}{r_0} - 1\right). \tag{23}$$

Equation 23 indicates that the term, r_0/aV_e determines the temperature profile of the ejected droplet. Based on the present experiments and some considerations

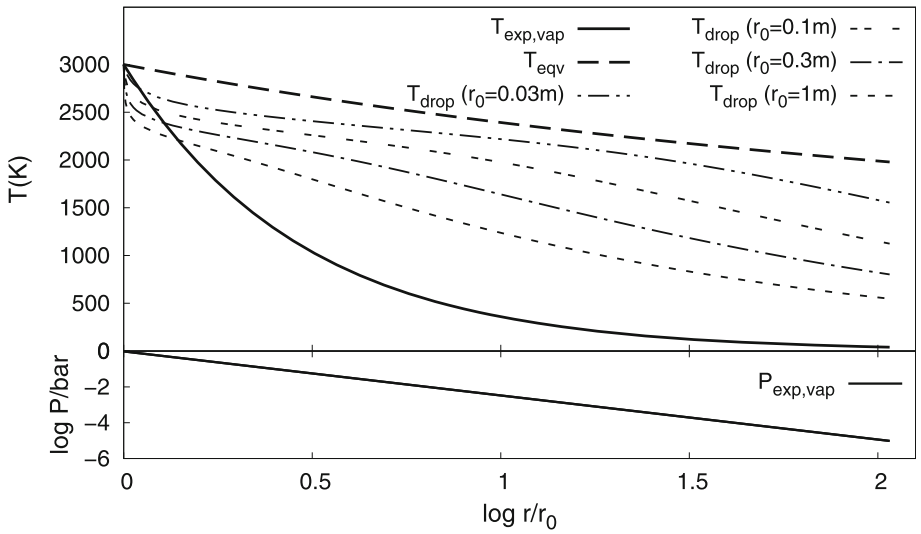

Fig. 10 Upper panel: Temperature profile of the expanding vapor ($T_{exp,vap}$: solid line), and those of ejected jet-droplets (T_{drop}) with a constant product of $aV_e = 2 \times 10^{-3}$ m^2 s^{-1}, starting from 3000 K as functions of the normalized radius, r/r_0. Four r_0 values (0.03, 0.1, 0.3, and 1 m) are selected for the radius of duston. The temperature profile of the expanding vapor is independent of the duston's normalized radius. T_{eqv} is the condensation temperature of a saturated silicate vapor whose pressure is equivalent to that of the expanding vapor, shown in the lower panel. Lower panel: Pressure profile of the adiabatically expanding vapor ($P_{exp,vap}$). T_{eqv} is higher than the droplet temperatures, meaning that the expanding vapor is always supersaturated for the droplets

(Appendix C), there is a good relationship between R_b (bubble radius) and V_e: $V_e = A\ exp(-\alpha R_b)$, ($A$ = 14.6 m s^{-1}, α = 330.3 m^{-1}) and between a and R_b : $log\ a = 1.1267\ log\ R_b - 0.4579$. The product, aV_e ranges from 1×10^{-3} to 2.75×10^{-3} m^2 s^{-1}, corresponding to the radius from $a = 8.5 \times 10^{-5}$ to 2.0×10^{-3} m for chondrules in ordinary chondrites.

Figure 10 shows temperature profiles of jet-droplet with the duston's radius as a parameter, $r_0 = 0.03$, 0.1, 0.3 and 1 m. Here we used $\rho = 3 \times 10^3$ kg m^{-3}, $\sigma = 5.6705 \times 10^{-8}$ J m^{-2} K^{-4}, $c_p = 1.458 \times 10^3$ J kg^{-1} K^{-1}, and $\Delta h_v^o = 1.936 \times 10^7$ J kg^{-1}. We have used enstatite liquid for values of c_p and Δh_v^o (Chase et al. 1985). We have also taken $aV_e = 2 \times 10^{-3}$ m^2 s^{-1} as average. A most notable feature is that the vapor is always super-saturated for jet-droplets, as T_{eqv} (condensation temperature of a saturated silicate vapor whose pressure is equivalent to that of the expanding vapor) is always higher than the droplet temperatures. This means that the vapor molecules that collide with jet-droplets effectively condense on them. Indeed, it points out that a quantitative analysis including the effect of droplet-vapor interaction is necessary.

Smaller dustons are covered with smaller vapor clouds, while ejection speeds of jet-droplets do not depend on duston size. It implies that the jet-droplets from small dustons suffer less from condensation of the vapor. With large dustons, on the other hand, droplets would cool down below their glass transition temperatures, ~1000 K, before their reaching the vapor condensation zone. In this case, the droplets would not be able to dissolve the condensed particles into their liquids, which are rich in volatiles such as Na and K, although they would condense more mass of moderately-volatile vapor by collision on the way. We therefore expect that we may be able to identify the size range of dustons that satisfies highly variable chemical and textural characteristics observed for chondrules. For a satisfactory argument, however, we need a quantitative estimate that considers exchange processes between jet-droplets and the vapor cloud in terms of mass, energy and momentum.

Model calculation of chondrule chemistry

(i) Semi-quantitative Approach We next evaluate the chemistry of jet-droplets, vapor and condensate that would evolve as a result of continuous evaporation of the MLB, viz., the molten surface of a duston. Our model predicts that chondrules consist of these three components because on their ways out from the vapor cloud, jet-droplets inevitably take vapor and condensate into their liquid masses. The question is when in the evaporative evolution of MLB they are ejected and how much uptake of vapor and condensate is possible. Another question is about characterization of dustons that should be a primary source of chondrules. We assume dustons to be dense aggregates of primordial dust which has the same elemental composition as that of the rocky component of the Sun or of CI chondrite. The elemental composition alone, however, is not enough to characterize dustons since their chemical or redox states must be specified.

The initial materials in our experiments, L^{sil} and Allende, included the ten oxide elements for analyses: Na, Mg, Al, Si, K, Ca, Ti, Cr, Mn and Fe, which are most abundant in CI (except for extreme volatiles and organic elements). We have found that the relative volatilities of the ten elements determined from the L200 experiments are most suitable for further use ("Application of relative volatilities to an arbitrary MLB: self-consistency test" section). All the nine elements except Fe are stable as oxide in normal redox environments assumed in PPD, but Fe would take various redox states such as oxides, sulfides, and metal. When melted, the oxides including Fe-oxide form one silicate liquid, but Fe metal and sulfides do not. Hence we take FeO content in the silicate as a parameter.

In the following analyses, we adopt the above-mentioned ten elements having CI abundance ratios on molar basis (Lodders 2003) and normalize the composition to 100 mol% in total. This is called our CI composition. The FeO content in our CI composition is adjusted as follows. We define f_s ($\leq$1) as the fraction of Fe that exists as oxide in the total Fe in our CI composition. This operation makes the total oxide mol% becomes less than 100, then it is normalized to 100 mol%. The normalized composition is different from our CI composition in Fe content but otherwise keeps CI abundance ratios among other nine elements. We call it CI^{sil}, as it represents a silicate composition when melted. Naturally CI^{sil} with $f_s = 1$ is identical to our CI composition.

We investigate the evaporative chemical fractionation of primordial dust with CI^{sil} as initial composition for f_s values 0.01, 0.1, 0.3, 0.5 and 1, assuming that it occurred in PPD environment at temperatures high enough to cause boiling. We use the relative volatilities for the ten elements determined from the L200 experiments and apply them to CI^{sil} composition, as is done in "Application of relative volatilities to an arbitrary MLB: self-consistency test" section for L^{sil}. We also note that the relative volatilities are properties that are insensitive to temperature variations as explained in "Definition of relative volatility and mathematical method of its derivation" section. This makes it logically sound for them to be applied to chondrules as their exact formation temperatures are not known but for being in the boiling range. Given the initial composition of MLB (X_i for Si and X_j for other nine elements), viz., CI^{sil}, a combination of Eqs. 12 and 15 gives a next set of composition (X_i' and X_j') for MLB after an infinitesimal evaporation, which in turn is used for a next step of evaporation and so on. In reality, a small but finite evaporation is imposed by setting the step index

$q = 1.005$-1.001 to be applied to each step of evaporation. A small $(q - 1)$ is required at large VD% or at high Al concentration in MLB for keeping a good precision in the approximation. At any step of evaporation jet-droplets may be produced from MLB, thus they have the same composition (X_i and X_j) as that of MLB at their ejection moment. Equations 16 and 17 give compositions of differential vapor and integrated vapor, respectively, in each iteration step. The differential vapor corresponds to the vapor of the vapor cloud at every moment of evaporation, which jet-droplets may travel through. The integrated vapor is the total vapor that accumulates from the start until a current evaporation step is reached, and corresponds to a bulk of condensed particles distributing near the border of the vapor cloud, which jet-droplets may go across.

Figure 11 shows concentrations (Na, Si and Fe) in jet-droplet, differential vapor and integrated vapor as a function of Mg concentration, in each of iteration step. In the same figures, chemical compositions of all chondrules in all types of chondrites (in so far as we surveyed) are plotted (see Appendix D for the sources of chondrule data). The composition of MLB evolves from CI^{sil} to Mg-rich one till Mg reaches 55.8, 57.5, 58.3, 59.2 and 59.7% (corresponding to $f_s = 1$, 0.5, 0.3, 0.1 and 0.01, respectively), where it turns to Mg-poorer one. The overturn is the effect of Ca enrichment as explained in "Relative volatilities of Mg and Fe" section. The Na, Si and Fe concentrations in MLB decrease continuously as evaporation proceeds. The Na concentration of differential as well as integrated vapor starts with ~58% (which is scaled out in the figures) and decreases monotonously as evaporation proceeds. The Fe and Si concentrations in the vapor (both differential and integrated) increase to their maximum values then decrease monotonously.

The triangle in each of Fig. 11 consists of the three tie lines between the compositions of the jet-droplet, differential vapor and integrated vapor at a specified evaporation step, in order to show an example that the chondrule compositions inside the triangle can be expressed by combination of the three components. It is, however, only a binary expression (e.g., Mg-Na) and does not guarantee that the same chondrules are enclosed in the triangle at the same evaporation step in another binary system (e.g., Mg-Si). This problem is completely removed in a quantitative treatment described in "(ii) Quantitative Approach" section.

Yet we emphasize the two points. 1) The composition space which combinations of the three components with variable evaporation degrees (VD%) and f_s values define appears to cover the entire space in which chondrules distribute. 2) A wide f_s range, 0.0-0.7 is required to cover all chondrules. The first point supports our hypothesis that chondrules were jet-droplets which subsequently reacted with vapor and condensate in the vapor cloud. The second point implies that the primary CI-composition dust which made dustons was quite variable in redox state, imposing a rather strong constraint on characterization of primordial dust. These points are reinforced in the following section.

(ii) Quantitative Approach We wish to calculate the chemical compositions of the three components and their mixing ratio that reproduce chemical compositions of

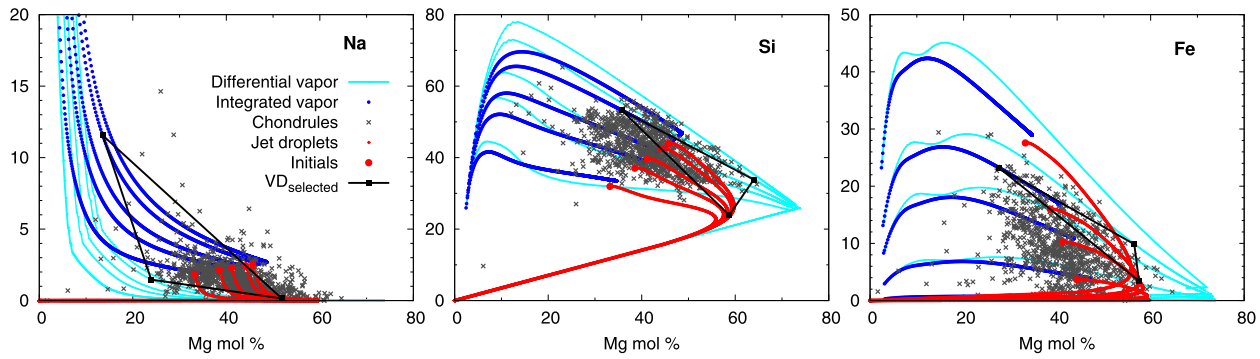

Fig. 11 Binary diagrams showing that a majority of real chondrules (crosses) is covered by the composition space defined by combinations of the three components, jet-dropet (in red), differential vapor (in light blue) and integrated vapor (in deep blue), that evolve by evaporation of the primordial silicates. Trajectories of chemical compositions (mol%) calculated for the three components are shown separately for five different initial CI^{sil} compositions with different f_s values, 0.01, 0.1, 0.3, 0.5 and 1. For the sake of visual clarity the parameter f_s is not shown in the figures; in the two left-most figures, a smaller f_s corresponds to higher concentrations in Mg, Na and Si for all three components; in the right-most figure, a smaller f_s corresponds to lower Fe concentration. Open triangle in each figure connects the three components that coexist at a specified evaporation step (or VD%) for the same f_s value, in order to show the composition space that can be expressed by combination of the three components. Such examples are shown: in the left, middle, and right figure, the triangle corresponds to f_s & VD = 0.1 & 20.1%, 0.1 & 63.3%, and 0.5 & 63.3%, respectively. 'Chondrules' are compositions of real chondrules from all types of chondrites analyzed so far (see Appendix D for their data source). 'Initials' are initial compositions, CI^{sil} corresponding to the five selected f_s values

silicate chondrules, by solving five simultaneous linear equations,

$$A_{m,n}F_n = B_m \ (m = 1\text{–}5 \quad \text{and} \quad n = 1\text{–}5). \tag{24}$$

Here B_m represents a molar fraction of element m = 1-4 (Na, Mg, Al and Si in ascending order) in a silicate chondrule. The basis of molar fraction is the ten elements as described before. $B_5 = 1$. F_n, an unknown to be determined, represents a mixing proportion (in molar basis) of the five components n = 1-5 (1: jet-droplet, 2: differential vapor, 3: integrated vapor, 4: final integrated vapor, and 5: our CI). By definition $\sum_n F_n = 1$. $A_{m,n}$ is a matrix to describe molar fractions of Na, Mg, Al and Si (m = 1-4) among the ten elements in each of the five components (n = 1-5). $A_{5,n} = 1$ (n = 1-5).

$A_{m,n}$ (m = 1-4; n = 1-3) can be obtained by calculating the evaporative chemical fractionation starting with CI^{sil}, similar to the one described in "(i) Semi-quantitative Approach" section, at any specified evaporation step (or VD%) and for any specified f_s as a parameter. $A_{m,4}$ (m = 1-4) is a chemical composition of the 'final' integrated vapor, viz., that of the total condensates that accumulate by the end of evaporation process from the MLB. It is distinguished from the composition of an integrated vapor that accumulates as condensates by a specified evaporation step, while more evaporation from the MLB is still to go. $A_{m,5}$ (m = 1-4) is the chemical composition of our CI as described in "(i) Semi-quantitative Approach" section.

Among the five components, only the first three components (n = 1-3) are needed to make chondrules. The two extra components (n = 4 and 5) are ones for making a matrix of chondrite. Equation 24 is originally devised for reproducing bulk composition of chondrites. The use of Eq. 24, however, is quite beneficial for reproducing chondrule compositions because the four elemental concentrations (Na, Mg, Al and Si) in chondrule composition instead of two can be used as constraints for solving the equation by finding a solution that imposes $F_4 = F_5 = 0$. It extremely enhances precision since the fifth element, Fe is already parameterized with f_s, leaving the five minor elements unconstrained. Although Ca is relatively abundant among the five minor elements, it is too refractory to fractionate from Al for a moderate evaporation degree (VD<95%) which appears to be appropriate for most chondrules. Therefore, the Ca/Al ratios of chondrules should be constant, viz., equal to that of the CI chondrite, if the original composition before their evaporative fractionations is CI^{sil}. It means that the Ca concentrations in chondrules cannot be a constraint to determine the VD% of chondrules. The remaining four elements, K, Ti, Cr and Mn, if combined, amount to less than 1 mol%, thus hardly affect the concentrations of other six elements when the total mol% of the ten oxides is normalized to 100. Besides, these minor elements had better not be included in the constraints because their concentrations are usually close to and sometimes below their detection limits in ordinary EPMA analyses on chondrules. For these reasons, we use the concentrations of the four elements, Na, Mg, Al and Si in chondrules as the constraints, and the parameter f_s for the initial FeO concentration in CI^{sil} in the following calculations.

Calculation proceeds with a step size $q = 1.001$ starting with CI^{sil} for a specified f_s, and obtains a set of $A_{m,n}$ at every step number. $A_{m,4}$ is temporarily assigned to $A_{m,3}$ that would obtain at twice the step number. This procedure inherits from the bulk chondrite fitting, as will be described in the companion paper (II). Here such an assignment has no influence on a final solution because F_4 and F_5 are eventually brought to zero.

Now Eq. 24 is solved at every step number to give the molar fractions F_n. Computation is repeated with f_s and step number as parameters so as to satisfy the following requirements: F_n (n = 1-3) to be all positive; F_4 and F_5 to be zero, or smaller than 0.005. We find a single solution which satisfies these conditions and identify f_s and step number (or VD%) for a given chondrule.

Chondrule chemical compositions used for the present numerical investigation are as follows: 88 chondrules in H3 chondrite (ALH-77299 analyzed by Ikeda 1983), 88 chondrules in E3 chondrite (Y-691 by Ikeda 1983), and 394 chondrules in total in L chondrites (Y-74191 by Kimura et al. 1979, ALH-77015 by Fujimaki et al. 1981; Nagahara 1981a; Ikeda 1983, and ALH-77249 by Kimura 1983).

We were able to determine the formation condition (f_s, VD%, F_1, F_2 and F_3) for majority of chondrules. For some chondrules, however, the calculation did not satisfy the aforementioned requirements and failed to give answers. The probability of giving right answers is 86% (76/88) for H3 chondrules, 75% (66/88) for E3 chondrules, and ~60% for L3 chondrules (50-80% depending on authors of EPMA analysis). A reasonably high probability confirms validity of our model.

Figure 12 (upper panel) shows frequencies of the chondrules as a function of VD%. The VD% ranges from 5 to 85 for H chondrules and from 10 to 90 for L chondrules. The mode is 25% for H and 35% for L. E chondrules distribute in a narrower range, 10-65%, with its mode 35%. These results implies the followings. 1) MLB, the source of chondrules, started to boil in early stages of heating and ejected jet-droplets. 2) Ejection of jet-droplets was most active in the middle stage of heating. 3) The ejection continued until evaporation of MLB reached 65-90 VD%. In our experiments (L200 and A200), ejection of jet-droplets started with VD ~5%. Therefore, it is suggested that there was a time lag for the MLBs before they ejected the first jet-droplets, during which temperature kept rising to their boiling points while evaporation proceeded up to 5-10% of their initial masses.

Figure 12 (lower panel) shows frequencies of the chondrules as a function of f_s. H and L chondrules distribute in the range from 0.05 to 0.5. Compared with L chondrules, H chondrules tend to have smaller f_s values. E chondrules have smaller f_s values, ranging from 0.025 to 0.15, with one chondrule with 0.4. Variable f_s values indicate various redox states in the initial materials, viz., dustons. A straightforward interpretation is that each duston had a different redox state or that duston was heterogeneous in distribution of the Fe oxide. Another possibility is that C-rich, refractory organic materials (CROMs) similar to CHON in comets (e.g., Kissel and Krueger 1987) and to IOM (e.g., Alexander et al. 2007) and organic nano-globules (e.g., Nakamura-Messenger et al. 2006) in carbonaceous chondrites, were incorporated into the duston and reacted with Fe oxides when it was heated to high temperatures. If CROMs were distributed heterogeneously inside the duston, they would have contributed to its internal heterogeneity in redox state. A big difference in the f_s range between E chondrules and H & L chondrules may be attributed either to a difference in the initial redox state of dustons or to a different abundance of CROMs in dustons.

Figure 13 (upper panels) shows the mixing proportion of the three components F_n ($n = 1$: jet-droplets, 2: differential vapor and 3: integrated vapor) determined for the same sets of chondrules as in Fig. 12. H and

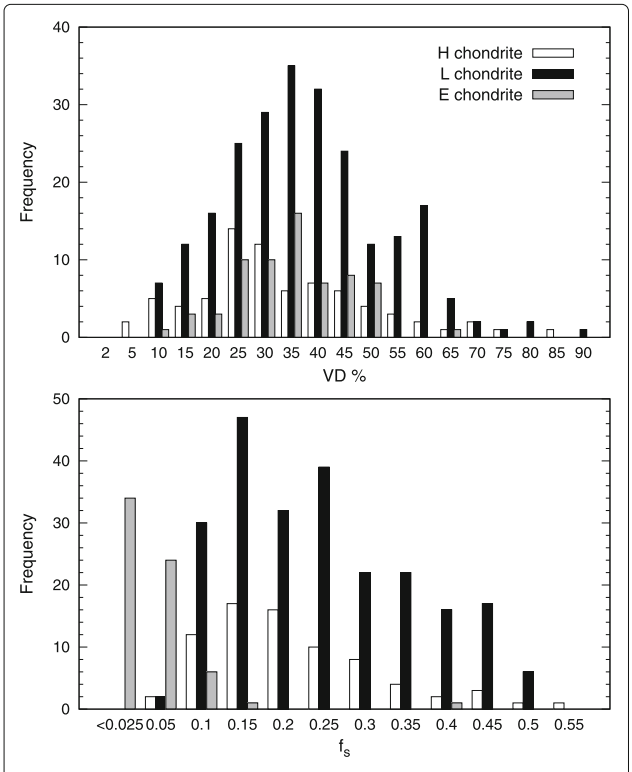

Fig. 12 Frequency of chondrules as functions of VD% and f_s

L chondrules show similar trends. The proportion of jet-droplets that contributes to the mass of chondrules decrease with increasing VD, while that of the integrated vapor increases. This trend is expected because more vapor should deposit near the border of the vapor cloud as VD increases. The proportion of the differential vapor shows no correlation with VD, and varies in wide range for both H and L. This indicates that the jet-droplets suffered from various degrees of condensation while traveling in the vapor cloud. Its cause is most likely a size difference among the jet-droplets as the efficiency of condensation is directly related to the mass/surface-area ratio. Another cause may be a size difference among dustons; a large duston should allow more time for a jet-droplet to travel through and also provide a denser vapor. E chondrules, on the other hand, have small proportions of integrated vapor compared to H and L. Instead, the proportion of differential vapor increases as VD increases, compensating the decrease in jet-droplet mass proportion.

Figure 13 (lower panels) shows concentration ratios of elements (Mg/Si and Na/Si) as a function of VD% for the same sets of chondrules. As VD increases, the Mg/Si ratio increases. The Na/Si ratio, however, has no correlation with VD, contrary to the common sense that volatile elements should deplete as evaporation proceeds. The observed trend can be explained by recondensation of the differential vapor and incorporation of the integrated vapor (as condensates) onto the jet-droplets.

The retention of alkaline elements by chondrules has been an issue of debate since chondrules experienced high temperatures at least above their melting points while they keep a level of alkaline concentrations similar to that of bulk chondrites which contain them. In the framework of the condensation model of liquid substances in PPD (e.g., Ebel and Grossman 2000), it has been shown that a dust enrichment (as high as 1000×) alone was not sufficient enough to retain alkaline elements unless the gas pressure in PPD was assumed as high as 10^{-3} bar. Hewins et al. (2005) have shown in their experiments that in a low density gas ($< 10^{-4}$ bar) such as in PPD, silicate liquids could not be held at their melting points, 1700-1900 K even for minutes without losing a significant amount of alkaline elements.

We, therefore, contend that ejection of jet-droplets into the vapor cloud that forms around a boiling duston could only explain the retention of both moderately-volatile elements such as Si, Fe, Cr and Mn and volatile elements such as Na and K in chondrules because the supercooled jet-droplets will immediately condense the supersaturated vapor, which is enriched in moderately-volatile-element, during their flights in the vapor cloud, and also will incorporate the fine condensates that are enriched in once evaporated volatiles and distribute near the vapor-cloud/disk-gas boundary. We also predict that

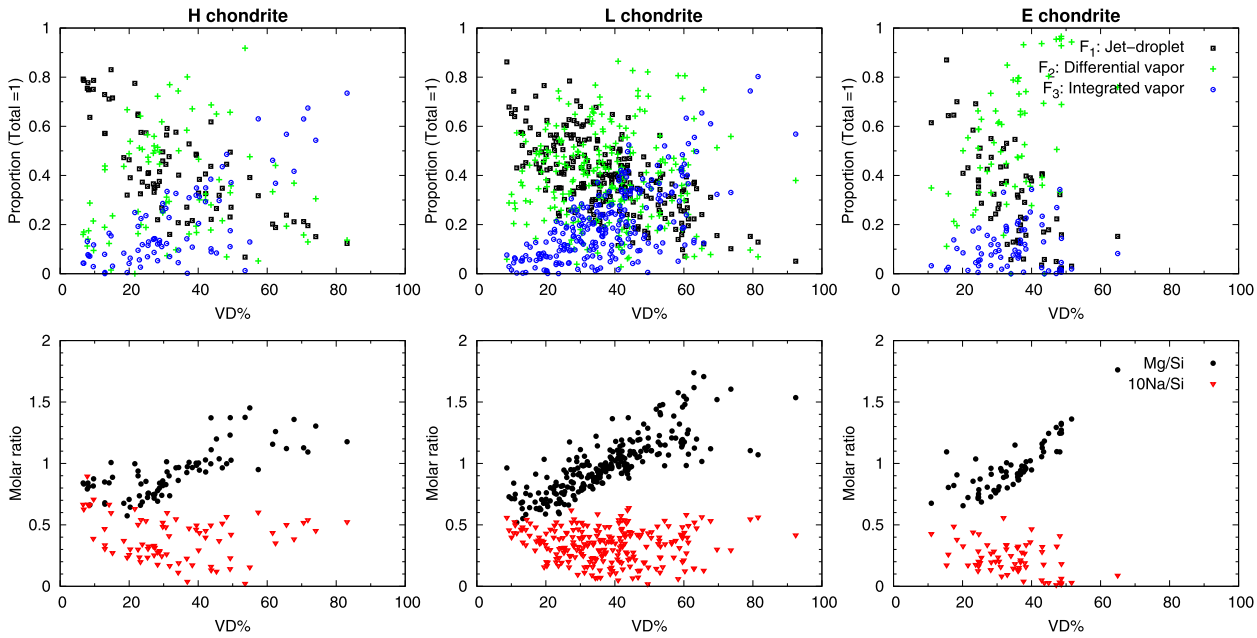

Fig. 13 Upper panels: Calculated proportions of the three components that constitute chondrules as a function of calculated VD%. Lower panels: Element/Si molar ratio in the chondrules as a function of calculated VD%

most chondrules were cold enough and completed their chemical makeup when they got out of the vapor cloud into the cold and thin environment in PPD.

We have focused our investigation on the chondrules that can be explained with our model calculations above, but a significant number of chondrules could not be fitted for their chemical compositions under the imposed constraints. The 14% in H chondrules, 25% in E chondrules, and 50% in L chondrules for the worst case have been left unfitted.

In the above numerical estimate, we have tacitly assumed that the chondrule composition data which were obtained with EPMA are reliable. But we have some doubt about this assumption. We discuss this issue in detail in Appendix E.

Origin of other features of chondrules

Our model naturally explains other recognized features of chondrules.

Petrographic textures of chondrules

Chondrules have many different petrographic textures, e.g., porphyritic, granular, barred, radial, cryptcrystalline, and glassy (e.g., Gooding and Keil 1981). Laboratory experiments have been performed to reproduce these various textures as a function of cooling rate of molten silicate charges in electric furnaces (e.g., Lofgren and Russell 1986; Hewins et al. 2005). The obtained cooling rates which correspond to unique textures have stimulated many theoretical scientists to evaluate the formation condition of chondrules and possible heat sources for melting (e.g., Boss 1996; Desch and Connolly 2002).

We disagree with the conventional belief about the cooling rates of chondrules. There is a critical problem in those experiments that negates the meaning of the derived cooling rates. The experiments almost unequivocally used a Pt-wire loop to hold a molten silicate charge with a help of surface tension, while in space there needs no support to hold chondrules. The holder provides nucleation centers for liquid to solidify and thus controls nucleation and crystallization process that follows (e.g., Hollomon and Turnbull 1953; Huisman et al. 1997).

Free-floating, laser-heating experiments using drop towers, high-speed gas flows or ultrasonic sound waves that levitate molten silicate charges remove the problem of preexisting solid nuclei (Nelson et al. 1972; Blander et al. 1976; Nagashima et al. 2008; Srivastava et al. 2010). These experiments have clearly shown that the supercooling degree of a melt charge is a crucial factor that determines petrographic textures upon its solidification. The fact indicates not only that previous electric-furnace, Pt-suspending, cooling experiments no longer apply to chondrules, but that precursory silicate droplets had been in a state of supercooling just before their solidification. From their petrographic insight, Kimura et al. (1979) have already concluded that chondrules are products of supercooled liquid silicates.

Our chondrule formation model postulates that the supercooling of jet-droplets was inevitable due to their fast cooling in the adiabatically expanding vapor with

no preexisting solid nuclei. Depending on the size and velocity of jet-droplets, the volume of the vapor clouds, and the temperature and density profile of the cloud, the jet-droplets would have experienced a various degree of supercooling. This might have created a variety of petrographic textures as seen in chondrules.

In their high-speed gas flow, laser-heating experiments, Nagashima et al. (2008) have pointed out that silicate liquids with high SiO_2 contents do not crystallize but becomes glasses irrespective of supercooling rates and that solid seeds were required to impact with the supercooled liquids to initiate their crystallization. In our model, we can predict a situation where supercooled jet-droplets were thrust into a zone with abundant condensed particles which would have grown in size large enough to act as seeds.

Relict grains in porphyritic chondrules

Porphyritic chondrules often contain relict grains (mostly olivine), which have been interpreted as evidence for incompleting melting during the chondrule formation (e.g., Nagahara 1981b ; Rambaldi 1981). We consider that the feature of relict grains observed in many of porphyritic chondrules is a by-product of our chondrule formation mechanism. We have two alternative explanations for it.

(i) The crystallization of a supercooled liquid droplet is accompanied by a release of large latent heat, a recalescence. It would raise the temperature of crystallizing chondrules above their melting temperatures momentarily, causing a remelting of just crystallized grains inside the chondrules. Whether it happens or not depends on the indicator $\Delta T_n/\Delta T_{hyp}$, where ΔT_n is the supercooling degree and ΔT_{hyp}, defined by $\Delta H_f/C_p^L$ (ΔH_f: heat of fusion, C_p^L: specific heat of liquid), is the hypercooling limit. If $\Delta T_n/\Delta T_{hyp}$ is smaller than 1, a remelting occurs. Accoring to the free-floating-crystallization experiment of a forsterite liquid by Srivastava et al. (2010), a porphyritic texture was obtained with the value ~0.7. Thus, a porphyritic chondrule could remelt momentarily by recalescence. If so, the omnipresent occurrence of relict grains (mostly olivine) is a natural consequence of the crystallization from the supercooled state. For a conclusive argument, however, we need further free-floating crystallization experiments that would use supercooled liquids with more realistic chemical compositions.

(ii) Alternatively, the relict grains are reminiscent of the incomplete remelting of the preexisting chondrules that solidified earlier. In our model, solidified chondrules emerge from the vapor cloud with a velocity of 1-20 m s^{-1}. Depending on the number density of dustons in space, which are simultaneously producing chondrules as jet droplets, chondrules may cross a neighboring hot vapor cloud and get partially remelted. In the companion paper (II), we investigate possibilities of various mechanisms for heating dustons. The probability of chondrules suffering from remelting would be surely dependent on the mechanisms.

Compound chondrules

In ordinary chondrites some fraction of chondrules, approximately 3%, are recognized as compound chondrules: a pair of chondrules that stick to each other (e.g., Wasson et al. 1995; Ciesla et al. 2004). To produce compound chondrules, either of the paired chondrules have to be in the liquid state (or at sub-solidus temperatures where some plastic deformation is possible) (Gooding and Keil 1981). Arakawa and Nakamoto (2016) argued that compound chondrules are likely to be formed through collisions among supercooled droplets. The presence of compound chondrules as high as 3% requires a high number density of chondrule precursory droplets for them to encounter frequently and also demands coexistence of both liquid and solid droplets in the same environment.

Our chondrule formation model predicts numerous jet-droplets, in the order of ten to thousand (cm^{-2} s^{-1}) being ejected from a duston surface, depending on conditions. The ejection direction is generally normal to the liquid surface but can be tilted up to 20° from the normal in water experiments (Rossodivita and Andreussi 1999). If the duston surface was uneven, jet-droplets from various crests, flanks and pits would cross each other's trajectories to enhance the chance of collision. If a number density of dustons was high, there might be also a chance that jet-droplets having already solidified pass through nearby vapor clouds and meet supercooled droplets.

The mutual collisional frequency would be calculated if proper populations of jet-droplets and dustons are specified, since the speed of jet-droplets is known as a function of their size from the present experiments (Appendix C).

Conclusions

This paper consists of two parts. The first part describes our newly designed experiment and its links to the chondrules in three ways:

(i) Boiling is a key to the formation of chondrules. Bursting of vapor bobbles on a surface of molten silicate creates a swarm of jet-droplets that are ejected from collapsed bubble cavities. These droplets exhibit a log-normal-like size frequency distribution, one of the major characteristics of chondrules. This discovery makes an extra size-sorting process redundant.

(ii) The formation mechanism of jet-droplets requires a dense and large (>3 cm across) silicate body as a source of chondrules. This conclusion is led by combination of the 1/10-1/5th law as to the size ratio of jet-droplet/bubble diameter and the maximum size of silicate vapor bubbles that can produce jet-droplets from their collapsed cavities. Many studies on water jet-droplets in the atmospheric

and oceanic science reinforce this conclusion. The silicate body is presumably an aggregate grown from primordial dust in PPD, which we name 'duston.'

(iii) The most important information that the present experiment provides is the full range of evaporation and condensation pathways for chondritic compositions. They are reduced to a newly defined quantity, 'relative volatilities' of elements, which can be used to predict chemical fractionations caused by evaporation and condensation for a silicate material having an arbitrary initial composition, including the CI composition.

The second part constructs a new formation model of chondrules with a particular emphasis on their chemistry, and highlights the following four aspects.

(iv) The source material for chondrules, viz., duston, has a CI-like chemical composition with its Fe oxide content f_s, viz., redox state, as a parameter.

(v) In PPD, a duston surface is exposed to a high flux of heat which makes its surface boil. We expect that a large, adiabatically-expanding vapor cloud develops around the duston and that supercooled jet-droplets travel though it. This creates a situation that jet-droplets, viz., chondrule nuclei, incorporate the supersaturated vapor and the fine condensates on their way out from the cloud.

(vi) By assuming that the three components (jet-droplets, differential vapor and integrated vapor) make a bulk of chondrule, we are able to predict chondrule compositions using relative volatilities of the ten elements determined by the experiment. First, we draw a whole range of trajectories in two-component composition spaces with f_s as a parameter, swept by each of the three components. This semi-quantitative approach shows that the three sets of composition trajectories cover the whole composition field occupied by real chondrules analyzed to today. The quantitative approach solves five simultaneous linear equations to give the exact chondrule composition, VD (vaporization degree) and f_s. Nearly 600 actual chondrules are fitted with this method, and ~75% of them give answers. They give the ranges in VD and f_s, as well as the mixing ratios of the three components, leading to the conclusion that chondrule chemistry is consistent with a single source material having CI-like composition, with a wide range of redox state (f_s = 0.02-0.55), with a wide range of vaporization degree (VD = 5-90%), and with a wide range in the mixing ratio of the three components.

(vii) Other features of chondrules, i.e., textures and compound chondrules, are explained as a natural consequence of the proposed model.

We have left an issue of a possible heat source in PPD, that had brought dustons to temperatures high enough to boil. This issue is handled with in the companion paper (II).

Appendix

(A) Ejection of silicate droplets by bursting of vapor bubbles

Bursting of sub-surface air bubbles in water generates two distinct types of water droplets (Lhuissier and Villermaux 2012). The bursting commences the moment the bubble's film cap ruptures in some mechanically weak place (Fig. 14a), usually along the pinching ring around the bubble. Due to the surface tension the film cap rolls up along its original curvature (Fig. 14b) to the other side of its perimeter (in ~100 μs after the rupture; Resch et al. 1986). In the meantime, the rolled film mass is fragmented to pieces of strings, then to multiple droplets by

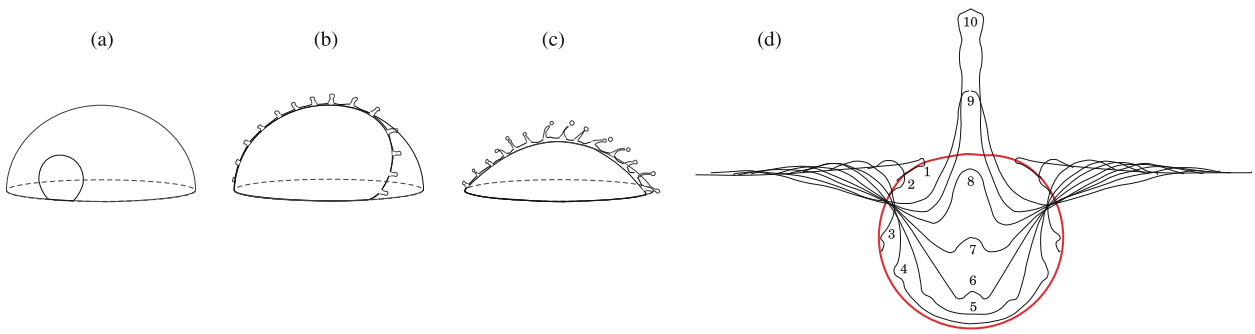

Fig. 14 **a**, **b** and **c**: schematic representation of bursting of an air bubble in succession (modified after Lhuissier and Villermaux 2012, figure 18). Only the film cap of the bubble is shown. **a** A pin-hole rupture in the film expands. **b** The rolled-up film starts to disintegrate into pieces of strings by Rayleigh-Taylor instability. **c** The instability continues to break up strings into multiple droplets, which is detached and ejected in tangential direction from the original film curvature, called film droplets. **d**: schematic representation of jet-droplet formation (modified after MacIntyre 1972, figure 1). The succession of profiles are ~1/6000 s apart, from label 1 through 10. The pseudo-circle in red indicates a shape of bubble just before the film rupturing. The profile 1 represents the moment the film cap is stowed away into its base perimeter by surface tension. The perimeter (now the edge of the gaping cavity) starts to collapse due to a continuous action of surface tension, generating a capillary wave that travels along the cavity wall to the bottom (profiles 2 through 5). The wave converges in the center to form an upward-moving jet (profiles 6 through 9). The jet starts to deform into nodes (profile 10) due to Savart-Plateau-Rayleigh instability (Duchemin et al. 2002)

Rayleigh-Taylor instability, and eventually ejected in tangential direction (Fig. 14c). They are called film droplets. Because the film rolling is very fast, a gaping cavity is left and its thin edge starts to collapse inward by surface tension, initiating a capillary wave (Fig. 14d: profiles 1-5). The wave converges at the bottom of the cavity and turns into a jet that protrudes in normal (viz., vertical) direction (Fig. 14d: profiles 6-10). The jet subsequently disintegrates into one to several droplets, depending on its momentum, by Savart-Plateau-Rayleigh instability (Duchemin et al. 2002). It takes 1-100 ms after the film cap rupturing for jet droplets to emerge (Resch et al. 1986). There are many works on the relationships between the bubble size and the droplet (both film and jet) properties (size, number and velocity) (Virij 1966; Resch et al. 1986; Blanchard and Syzdek 1988; Resch and Afeti 1991b, 1992; Spiel 1998; Wu 1994; Lhuissier and Villermaux 2012; Kientzler et al. 1954; Hayami and Toba 1958; Spiel 1995, 1997; Rossodivita and Andreussi 1999; Georgescu et al. 2002; Lee et al. 2011).

The diameters of jet-droplets are known experimentally and theoretically to be 1/10-1/5 of the diameters of the bubbles from which they are ejected (e.g., Kientzler et al. 1954; Hayami and Toba 1958; Duchemin et al. 2002). The number of droplets that produce from a single jet is one to six; it reduces to one when the bubble diameter is large, and increases up to six when it gets smaller. If the bubble diameter exceeds 5.4 mm for fresh water and 6.0 mm for seawater, no jet-droplet produces (Georgescu et al. 2002). This is related to the viscous dissipation of capillary wave when it travels along the cavity wall (Blanchette and Bigioni 2006). The number of film-droplets, on the other hand, is large, 1-110 (Speil 1998) and increases with the bubble size. The diameter of film-droplets is $<1/30$ of the bubble diameter. Since jet- and film-droplets are mutually different in their characters, it is rather easy to distinguish them.

In the early phase of our experimental research, we carried out several boiling experiments using a tungsten resistance heater in vacuum. By doping 3 wt.% carbon into the experimental charge (∼CI-chondritic composition), the liquid silicate boiled at 1500 °C due to the CO gas that formed by reaction of carbon with iron oxide. A high speed camera was available by courtesy of Dr. Arakawa, Institute of Low Temperature Science, Hokkaido University. In run# V1, we observed ∼500 bubble bursts in 10469 frames of image (shutter speed 1/5000 s; 2 s in total) and identified only 6 events in which a single droplet each was ejected. In run# V2, we observed ∼400 bubble bursts in 25124 frames (1/5000 s; 5 s) and identified 3 events two of which are a single shot of droplet, but one event produced three jet-droplets as well as six film-droplets (Fig. 15).

The six film-droplets ejected at the same time with velocity ∼3 m s^{-1} in a fan-like direction. The thickness of their trajectories is translated to their diameters, ∼40 μm and uniform. The three jet-droplets were various in size, and ejected in different directions due to gravity. The fastest of the three was ∼1 m s^{-1}. The slowest one was the largest in size, ∼180 μm in diameter. The bubble diameter just before its bursting is 1080 μm. Hence the largest jet-droplet is ∼1/6 of and the film-droplets are ∼1/27 of the bubble size, which conforms to the droplet/bubble ratios for water. The reason why the ejection frequency of droplets is so small compared to the number of bubble bursts can be explained by the high viscosity of liquid silicate at such a low temperature (1500 °C), which dampened capillary waves and also reduced film rolling speeds.

A high speed camera was unavailable for the present experiments that used laser beam heating. Instead we used a conventional video camera (frame rate = 30 fm s^{-1}; exposure time = 1/60 s). Experiments with a low laser power are suitable for observing jets owing to a low degree of halation, but jetting is limited to vicinity of the direct laser spot (∼10 o'clock direction). Figure 16a-c (run# 2; 65 W) shows elongated jets (due to the long exposure time) along with earlier split droplets (seen as elongated trajectories) on their extensions. Figure 16d-f shows jet-droplets in run# 39-2, 39-1 and 38 (all 100 W), respectively. Thin trajectories tend to elongate longer, indicating that smaller droplets have higher ejection velocities. A bunch of trajectories in very close proximity appears to originate in the same jet source. There are many such instances observed in these frames. It is possible that the source jet shifts its position while spewing droplets one after another. It is also possible that droplets with different masses and velocities take different paths due to gravity. Experiments with a high laser power (200 W) produce jet-droplets in all directions because the entire sample is kept above the boiling temperature, as shown in Fig. 16g&h (run# 83). A strong halation, however, shrouds their source jets. Rarely a number of droplets eject in a fan-like, synchronized fashion, suggesting them being film droplets from a single bubble burst, as shown in Fig. 16i (run# 83). Figure 16j (run# 32) shows a light-scattering cloud of condensed, ultra-fine particles that accumulates in a late phase of evaporation.

(B) Critical bubble radius for ejection of jet-droplet

Georgescu et al. (2002) obtained numerically critical bubble radii for twenty kinds of liquids (table 1 in their paper), including freshwater and seawater. Table 7 is an extended version of their table 1, where we have included three kinds of rock melts at three temperatures (# 22-29) with their physical properties. We have used data by Bottinga and Weill (1972) for viscosity and data by Nelson and Carmichael (1979) for densities, and extrapolated those to high temperatures. The surface tension, 0.4 N m^{-1}, is taken constant for all melts at temperatures for the following reasons. There are no pertinent

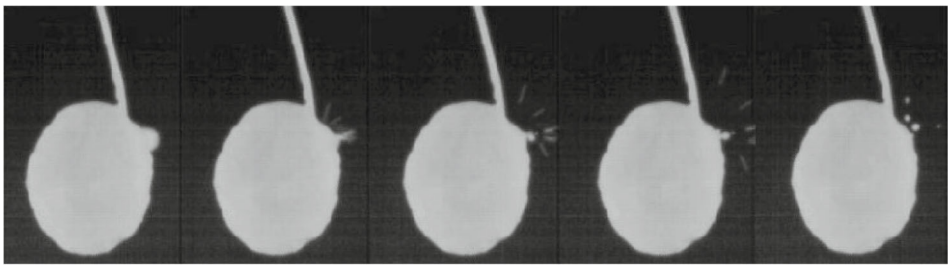

Fig. 15 High speed camera visions (1/5000 s apart) from left to right. Between the 4th and 5th frames, four frames are omitted. The sample charge (∼CI-chondritic composition doped with 3 wt.% carbon) is suspended with a PtRh wire and is in its total melting at 1500 °C. The horizontal width of the charge is ∼5 mm. A bulged bubble on the 1st frame is already ruptured on the 2nd frame, where multiple film-droplets are ejected while a jet is still developing from the center of the collapsed cavity. On the 3rd and 4th frames, the six film-droplets are spreading out in concert, while the first jet-droplet is detached from tip of the jet. Skipping four frames, the 5th frame shows three jet-droplets moving away from the mother liquid body. Their direction of motion is up and far side of the picture. The film-droplets are out of the 5th frame because they move fast

data for multicomponent rock melts. The surface tensions in binary silicate melts (e.g., MgO-SiO_2, CaO-SiO_2, MnO-SiO_2 and FeO-SiO_2) are similar in values and their temperature derivative is small (Turkdogan 1983). So we take that of $MgSiO_3$ (enstatite melt) ∼0.4 N m^{-1} at ∼1600 °C for all melts and temperatures.

The computed R_{cr} values by Georgescu et al. (2002) combined with Eq. 19 give wave numbers for critical bubbles. They are shown in Table 7 for twenty liquids. We have looked into the relationship between viscosity and (critical) wave numbers for these liquids and found a good linear correlation between log μ and log k as shown in Fig. 17.

$$log\ (k/\mathrm{m}^{-1}) = -0.6003\ log\ (\mu/\mathrm{Pa\ s}) + 2.1516. \quad (25)$$

Applying Eq. 25 we obtain (critical) wave numbers for the three kinds of rock melts as shown in the 2nd rightmost column of # 21-29 in Table 7. Then by applying Eq. 19,

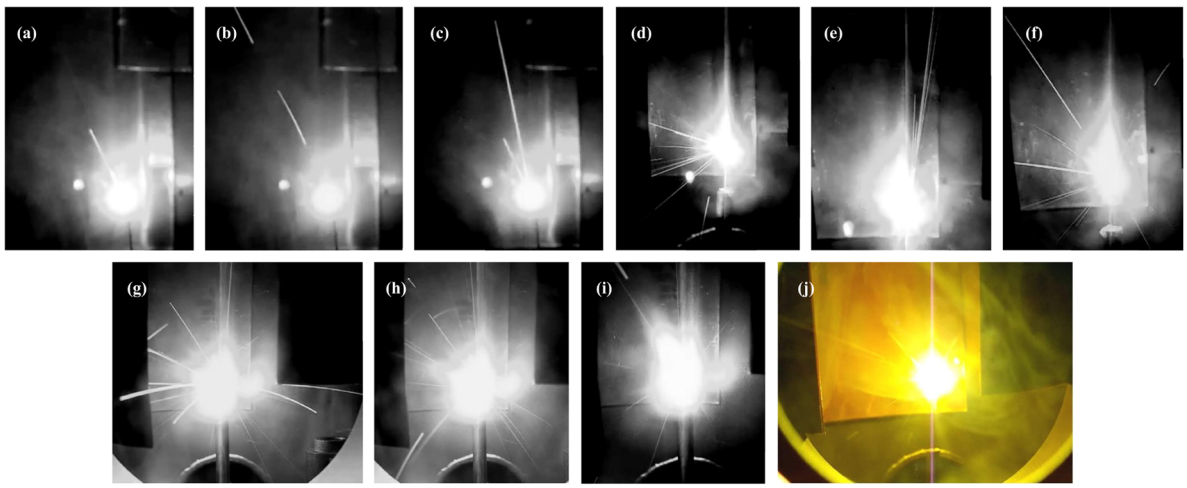

Fig. 16 Snapshots of jet-droplet ejection from the boiling sample. The video camera speed is 30 fm s^{-1}, and its exposure time is 1/60 s. **a**, **b** & **c**: run #2 (65 W). The central bright ball is an effect of halation. The actual sample diameter is about one half of the ball. The field of view is ∼35 mm across. In this low laser power (65 W) experiment only the laser spot and its vicinity is above boiling temperature, and hence jet-droplets are ejected in ∼10 o'clock direction where laser beam comes from. **a** and **b** are successive video frames. In **a**, the first jet-droplet is ejected while the jet is still extending for a second droplet. In **b**, the first and second jet-droplets are seen. The length of their trajectories and the exposure time give their velocities, ∼0.6 m s^{-1}. **d**, **e** & **f**: run #39-2, #39-1, and #38 (all 100 W), respectively. Thin trajectories tend to elongate longer, indicating that smaller droplets have higher ejection speeds. **g**, **h** & **i**: run #83 (200 W). Experiments with high laser power (200 W) produce jet droplets in all directions because the entire sample are kept above boiling temperature. In **g**, thick and bent trajectories of several jet-droplets indicate their large size. In **h**, thin, straight and elongated trajectories stand out, indicating smaller and faster droplets than in **g**. Rarely a number of droplets are ejected in a fan-like, synchronized fashion, suggesting them being film droplets from a single bubble burst, as shown in **i**. **j**: run #32 (200 W). In a late phase of evaporation as shown in **j**, a thick cloud of condensed, ultra-fine particles, a source of light-scattering, develops and circulates in convective motion

Table 7 Critical bubble radii for various liquids (modified after Georgescu et al. 2002, table 1)

#	Liquid type	Density ρ (kg m^{-3})	Surface Tension σ (N m^{-1})	Viscosity μ (Pa s)	log μ	Cr.bub.rad. exp.*1 R_{cr} (m)	Cr.bub.rad. comput.*2 R_{cr} (m)	Wave number (m^{-1}) calc.*3 log k	Wave number (m^{-1}) graph*4 log k	Cr.bub.rad. calc.*5 R_{cr} (m)
1	acetic acid	1046	0.0276	1.220E-03	-2.914	2.06E-03	2.32E-03	3.854	–	–
2	acetone	791	0.0233	3.240E-04	-3.489	2.37E-03	2.46E-03	4.156	–	–
3	aniline	1022	0.04267	4.466E-03	-2.350	–	2.04E-03	3.575	–	–
4	benzene	885	0.02888	6.470E-04	-3.189	–	2.42E-03	4.008	–	–
5	carbon tetrachloride	1594	0.0262	9.750E-04	-3.011	–	1.29E-03	4.142	–	–
6	CFC-113	1617	0.0199	9.600E-04	-3.018	1.34E-03	1.19E-03	4.133	–	–
7	distilled water	998.2	0.07274	1.002E-03	-2.999	2.70E-03	2.87E-03	3.983	–	–
8	ethanol	798	0.0228	1.194E-03	-2.923	1.84E-03	2.16E-03	3.814	–	–
9	e-w (2-98 wt%)	993	0.0655	1.090E-03	-2.963	2.29E-03	2.54E-03	3.978	–	–
10	g-w (85-15 wt%)	1220	0.0657	1.108E-01	-0.955	–	1.98E-03	2.742	–	–
11	g-w (79-21 wt%)	1210	0.0664	4.970E-02	-1.304	–	2.15E-03	2.951	–	–
12	g-w (70.5-29.5 wt%)	1185	0.0676	2.350E-02	-1.629	–	2.34E-03	3.143	–	–
13	g-w (65-35 wt%)	1170	0.0683	1.540E-02	-1.812	–	2.60E-03	3.234	–	–
14	g-w (50-50 wt%)	1130	0.0694	5.980E-03	-2.223	–	2.72E-03	3.493	–	–
15	i-propanol	791	0.0214	2.420E-03	-2.616	1.40E-03	1.42E-03	3.721	–	–
16	methanol	804	0.0226	5.600E-04	-3.252	2.22E-03	2.40E-03	4.003	–	–
17	mineral oil	840	0.029	1.700E-02	-1.770	–	2.18E-03	3.085	–	–
18	n-butanol	816	0.0247	2.980E-03	-2.526	1.25E-03	1.28E-03	3.716	–	–
19	n-propanol	805	0.0237	2.190E-03	-2.660	1.50E-03	1.87E-03	3.687	–	–
20	seawater (NaCl 3.4%)	1024	0.08023	1.126E-03	-2.948	3.00E-03	2.94E-03	3.960	–	–
21	peridotite 3000 °C	2462	0.4	4.490E-04	-3.348	–	–	–	4.161	1.275E-02
22	dunite 3000 °C	2577	0.4	3.700E-04	-3.432	–	–	–	4.212	1.329E-02
23	enstatite 3000 °C	2503	0.4	3.910E-03	-2.407	–	–	–	3.597	1.036E-02
24	peridotite 2700 °C	2508	0.4	9.350E-04	-3.029	–	–	–	3.970	1.196E-02
25	dunite 2700 °C	2612	0.4	7.470E-04	-3.127	–	–	–	4.029	1.248E-02
26	enstatite 2700 °C	2475	0.4	7.070E-03	-2.151	–	–	–	3.443	9.714E-03
27	peridotite 2400 °C	2556	0.4	2.290E-03	-2.640	–	–	–	3.736	1.104E-02
28	dunite 2400 °C	2652	0.4	1.770E-03	-2.752	–	–	–	3.804	1.154E-02
29	enstatite 2400 °C	2458	0.4	1.460E-02	-1.837	–	–	–	3.254	9.007E-03

Note. g-w: glycerol-water solution. e-w: ethanol-water solution. Cr.bub.rad.: Critical bubble radius.
exp.*1: experimentally obtained values, see references in Georgescu et al. (2002). comput.*2: numerically obtained by Georgescu et al. (2002)
calc.*3: calculated from R_{cr} with Eq. 19. graph*4: obtained from μ with Eq. 25. calc.*5: calculated from k with Eq. 19

we obtain R_{cr} for these rock melts at three temperatures as shown in the rightmost column in Table 7 and also in Table 6.

(C) Relationship between jet-droplet size and its ejection speed

We attempt to estimate ejection speed of jet-droplets from the silicate liquid, with the known relationship between droplet size and its ejection speed determined for water jet-droplets as a guide. The source of energy for giving rise to the formation of jet-droplets is the sum of the surface energy and the potential energy stored in the gaping cavity formed just after bursting of a bubble. In PPD, the potential energy is ignored due to its micro-gravity environment, and on earth it can be ignored for a small bubble because the surface tension dominates. In the following, the cavity is assumed to be a hemisphere with its radius R_b, then the surface energy stored in the cavity is $2\pi R_b^2\sigma$, where σ is the surface tension of the liquid. Subtracting the surface energy needed to mend the liquid surface to

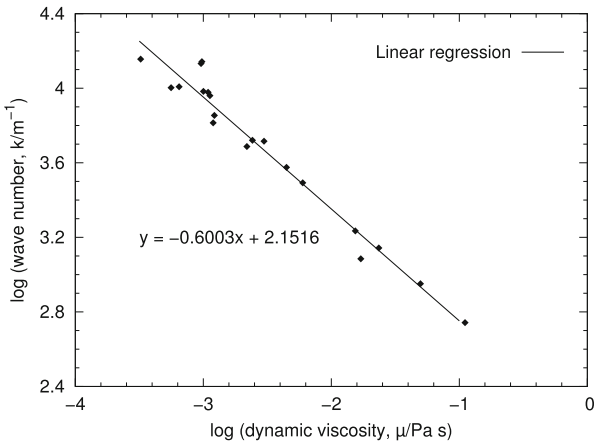

Fig. 17 log μ versus log *k* of various liquids in Table 7

a flat plane $\pi R_b^2 \sigma$, the available energy for jet-droplet formation is $\pi R_b^2 \sigma$. Assuming n droplets of equal radius a to be produced in a single bursting event, a total $4\pi a^2 \sigma n$ is required to form droplets. The remaining energy is available for the kinetic energy of droplet ejection. Neglecting viscous dissipation during the whole process, the ejection speed of the droplets is given by

$$V_e = \left(\frac{3}{2} \frac{\sigma}{\rho} \frac{1}{a} \left(\frac{\phi^2}{n} - 4 \right) \right)^{1/2}. \quad (26)$$

Here ρ is density of the liquid and $\phi = R_b/a$ is the size ratio of bubble/droplet.

According to the experiments by Spiel (1997), five jet-droplets of 20 μm in radius eject in bursting of an air bubble of radius 200 μm. Substituting $a = 2 \times 10^{-5}$ m, $\phi = 10$, $n = 5$, $\sigma = 0.07274$ N m^{-1} and $\rho = 1000$ kg m^{-3}, into Eq. 26, V_e is calculated to be 9.3 m s^{-1}. This is comparable to the value 9.2 m^{-1} that is obtained by extrapolation of the droplet radius vs. ejection speed relation of Spiel (1997), indicating that Eq. 26 is a good approximation. Obviously gravity and viscous dissipation has little effect on ejection of jet-droplets from a small bubble.

The same procedure is applied to the silicate liquid and jet-droplets therefrom. Substituting $\sigma = 0.4$ N m^{-1} and $\rho = 2550$ kg m^{-3} (at 3000 K) and taking the same value for a, ϕ and n, we obtain $V_e = 13.7$ m s^{-1}.

For large bubbles, it is known experimentally (Resch and Afeti 1991b; Suzuki and Mitachi 1995) and theoretically (Georgescu et al. 2002) that jet-droplets do not form due to viscous dissipation for the bubble radius $> 3 \times 10^{-3}$ m for water. A droplet that marginally form at $R_b \sim 3 \times 10^{-3}$ m has a speed ~0.1 m s^{-1} (Hayami and Toba 1958; Spiel 1995). Spile (1997) obtained the relationship between bubble radius and ejection velocity of jet-droplets as $V_e = 12.12\ exp(-1.390 \times 10^3 R_b)$. Application of this equation to $R_b = 3 \times 10^{-3}$ m and $a = 6 \times 10^{-4}$ m, gives $V_e = 0.2$ m s^{-1}, in good agreement with the observation. Here we used $\phi = R_b/a = 5$ for large bubbles.

In "Evidence for chondrules being jet-droplets" section, we derived the critical bubble radius $R_{cr} = 1.25 \times 10^{-2}$ m for production of jet-droplets from the silicate liquid. We assume that a speed of jet-droplet that may eject by bursting of the critical bubble is 0.2 m s^{-1} just as from water. By fitting an attenuation relation of the form $V_e = A\ exp(-\alpha R_b)$ to the two sets of (R_b, V_e), viz., (2×10^{-4}, 13.7) and (1.25×10^{-2}, 0.2), we obtain $A = 14.6$ m s^{-1} and $\alpha = 330.3$ m^{-1}. We further assume that $\phi = 10$ for $a = 2 \times 10^{-4}$ m and $\phi = 5$ for $a = 1.25 \times 10^{-2}$ m, and obtain the relation, $log\ a = 1.1267\ log\ R_b - 0.4579$. These two equations are used in "Vapor cloud model" section.

We have found that the value α is very close to $4/R_{cr}$ for yet unknown reason. In case of water, the computer simulation by Georgescu et al. (2002) gave $R_{cr} = 2.87 \times 10^{-3}$ m, which result in $4/R_{cr} = 1.393 \times 10^3$ m^{-1}, being very close to the value $\alpha = 1.390 \times 10^3$ m^{-1} by Spiel (1997) experiments. For our silicate liquid (dunite or peridotite), $4/R_{cr} = 4/0.0125 = 320$ m^{-1}, which is close to $\alpha = 330.3$ m^{-1} as obtained above. If this relation holds for any liquid, we may write $V_e = A\ exp(-R_b/R_b^*)$; $R_b^* = R_{cr}/4$ (R_b^*: bubble scale radius for jetting). It also indicates that the ejection speed has an upper limit: $A = 12.1$ m s^{-1} for water and $A = 14.6$ m s^{-1} for silicate liquid.

(D) Data sources of chondrule compositions

Table 8 lists references of chondrule chemical compositions used for the numerical investigation in "Model calculation of chondrule chemistry" section.

(E) Assessment of chondrule analyses

A bulk elemental, X-ray analysis with Electron Probe Micro-Analyzer on chondrules is made on a cross-section of chondrules as they expose by cutting their parent meteorites. Two fundamental problems are attached to this method for determining the bulk composition of chondrules.

1) A mineral proportion that reveals on a cross-sectional area does not necessarily represent its real proportion in an entire chondrule volume. Chondrules generally consist of several mineral species including glass. They have their own unique chemical compositions. In many cases they appear as relatively large crystals and distribute rather heterogeneously inside chondrules. Therefore, a chance cross-section may not represent their average proportions in the bulk of a chondrule. On the other hand, chondrules with a finer petrographic texture also exist in large number. In that case a cross-section is not a bad manifestation of bulk chondrules. Whether or not a cross-section represents a true bulk mineral proportion is hard to be evaluated especially after cross-sectioning.

Table 8 Data source of chondrule compositions

Chondrite type	Chondrite name	Reference
H3	ALH 77299	Ikeda (1983)
H3	Y 790986	Ikeda (1983)
L3	ALH 77015	Fujimaki et al. (1981), Nagahara (1981a), Ikeda (1983)
L3	ALH 77249	Kimura (1983)
L3	Y 74191	Ikeda and Takeda (1979), Kimura et al. (1979)
LL3	ALH 764	Ikeda (1980)
LL3	Semarkona	Jones and Scott (1988), Jones (1990), Jones (1996), Hewins et al. (2012)
EH3	Y 691	Ikeda (1983)
CM2	EL-Quss Abu Said	Hezel and Palme (2010)
CO3	ALH-77003	Ikeda (1982)
CO3	Y 790992	Ikeda (1983)
CO3	Kainsaz	Hezel and Palme (2010)
CV3	Efremovka	Hezel and Palme (2010)
CV3	Allende	Isobe et al. (1986)
CR2	Renazzo	Hezel and Palme (2010)

2) ZAF and Bence & Albee correction methods for X-ray intensities (e.g., Reed 2005) are optimized for a small electron beam (micro-probe) diameter because they assume a uniform composition. A bulk chondrule analysis with EPMA, however, uses in almost all cases a large (viz., defocused) electron beam, 30-100 μm in diameter, depending on analysts, to cover a large area as possible in a single analysis. Usually many analyses are made to cover a whole cross-sectional area and averaged for a bulk composition. A large electron beam excites X-rays from a large area of sample which may encompass more than two compositionally different phases or minerals, which violates normal matrix corrections in the built-in computation program and may become a source of large errors. In order to overcome this problem, various compensation procedures have been developed (e.g., Albee et al. 1977; Bastin et al. 1983). Ikeda (1980) determined calibration coefficients for correcting broad-beam effects element by element, by synthesizing artificial mineral assemblages of known chemical compositions similar to chondrules, and calibrating apparent concentrations of elements determined with EPMA with known values. Without such broad-beam corrections and depending on elements, an error of a few tens of percent is not uncommon (Albee et al. 1977; Ikeda 1980).

Our numerical investigation on chondrules outlined above had originally included Y-74191 (L3) chondrules analyzed by Ikeda and Takeda (1979). Their analyses, however, had given unusually high concentrations in Na and Al compared to other L3 chondrules, obviously due to no correction for broad-beam analysis. Our calculation was capable of determining the formation conditions only for 6 out of 43 chondrules (viz., 14%) whose compositions had been provided by Ikeda and Takeda (1979). This unusually low percentage reconfirms the importance of the broad (defocused) beam corrections. These six chondrules are not included in Figs. 12 and 13.

Although it is not an analytical problem, there is an important factor that alters primary chemical compositions of chondrules: alteration or reactions of chondrules with matrix materials that are usually postulated to have occurred in meteorite parent bodies. The reason why we chose petrographic type 3 chondrites for our research is that they are least-altered among those which belong to the same chemical type (Van Schums and Wood 1967).

Abbreviations

MLB: Mother liquid body; VD: Vaporization degree; CROMs: C-rich, refractory organic materials, CAI: Calcium-aluminum-rich inclusion, IOM: Insoluble organic materials

Acknowledgements

We are greatly indebted to the members of the Planetary and Space Science group, Hokkaido University, for their valuable comments throughout this work and to Dr. A. Kouchi, Institute of Low Temperature Science, Hokkaido University for useful discussion. The chemical analysis on the experimental products in this work were made at Pheasant Memorial Laboratory for Geochemistry and Cosmochemistry, Institute for Study of the Earth's Interior, Misasa. We greatly appreciate Dr. E. Nakamura and his staffs in Misasa for providing such an opportunity. We wish to thank Mr. Z. Nakamura and his men of Tanaka Ltd. for their continuous and sincere support. Machine shop in Hokkaido University is acknowledged for their technical helps. We thank the anonymous reviewers for their careful reading of our manuscript and their comments and suggestions.

Authors' contributions

YN designed the experimental set-up, conducted the experiments, performed the analysis, and wrote the paper. AH supervised the study, conceived the model, made the numerical calculations, and wrote the paper with YN. The author(s) read and approved the final manuscript.

Funding

This research received no specific grant from any funding agency in the public, commercial, or not-for-profit sectors.

Availability of data and materials
Experimental data is available from the corresponding author upon reasonable request.

Competing interests
The authors declare that they have no competing interest.

Author details
[1]Department of Cosmosciences, Hokkaido University, N10 W8, Sapporo 060-0810, Japan. [2]Suns & Fishermen Society, Sapporo, Japan.

Received: 11 November 2019 Accepted: 17 May 2020
Published online: 11 September 2020

References

Albee AL, Quick JE, Chodos AA (1977) Source and magnitude of errors in "broad-beam analysis" (DBA) with the electron probe [abstract]. LPSC:1003. http://adsabs.harvard.edu/full/1977LPI.....8....7A. Accessed 01 Jul 2020
Alexander CMOD (2001) Exploration of quantitative kinetic models for the evaporation of silicate melts in vacuum and in hydrogen. Meteorit Planet Sci 36:255–283. https://doi.org/10.1111/j.1945-5100.2001.tb01870.x
Alexander CMOD (2002) Application of MELTS to kinetic evaporation models of FeO-bearing silicate melts. Meteorit Planet Sci 37:245–256. https://doi.org/10.1111/j.1945-5100.2002.tb01107.x
Alexander CMOD, Fogel M, Yabuta H, Cody GD (2007) The origin and evolution of chondrites recorded in the elemental and isotopic compositions of their macromolecular organic matter. Geochim Cosmochim Acta 71:4380–4403. https://doi.org/10.1016/j.gca.2007.06.052
Arakawa S, Nakamoto T (2016) Compound chondrule formation via collision of supercooled droplets. Icarus 276:102–106. https://doi.org/10.1016/j.icarus.2016.04.041
Bastin GF, van Loo FJJ, Vosters PJC, Vrolljk JWGA (1983) A correction procedure for characteristic fluorescence encountered in microprobe analysis near phase boundaries. Scanning 5:172–183. https://doi.org/10.1002/sca.4950050402
Blander M, Planner HN, Keil K, Nelson LS, Richardson NL (1976) The origin of chondrules: experimental investigation of metastable liquids in the system Mg_2SiO_4-SiO_2. Geochim Cosmochim Acta 40:889–896. https://doi.org/10.1016/0016-7037(76)90137-X
Blanchard DC, Syzdek LD (1988) Film drop production as a function of bubble size. J Geophys Res Oceans 93(C4):3649–3654. https://doi.org/10.1029/JC093iC04p03649
Blanchard DC (1989) The ejection of drops from the sea and their enrichment with bacteria and other materials: A review. Estuaries 12:127–137. https://doi.org/10.2307/1351816
Blanchette F, Bigioni TP (2006) Partial coalescence of drops at liquid interfaces. Nat Phys 2:254–257. https://doi.org/10.1038/nphys268
Blum J, Wurm G (2008) The Growth Mechanisms of Macroscopic Bodies in Protoplanetary Disks. Annu Rev Astron Astrophys 46:21–56. https://doi.org/10.1146/annurev.astro.46.060407.145152
Blum J, Gundlach B, Krause M, Fulle M, Johansen A, Agarwal J, von Borstel I, Shi X, Hu X, Bentley MS, Capaccioni F, Colangeli L, Della Corte V, Fougere N, Green SF, Ivanovski S, Mannel T, Merouane S, Migliorini A, Rotundi A, Schmied R, Snodgrass C (2017) Evidence for the formation of comet 67P/Churyumov-Gerasimenko through gravitational collapse of a bound clump of pebbles. Mon Not R Astron Soc 469(S755-S773). https://doi.org/10.1093/mnras/stx2741
Blum J (2018) Dust Evolution in Protoplanetary Discs and the Formation of Planetesimals. Space Sci Rev 214(52). https://doi.org/10.1007/s11214-018-0486-5
Boss AP (1996) A concise guide to chondrule formation models. In: Hewins RH, Jones R, Scott E (eds). Chondrules and the Protoplanetary Disk. Cambridge University Press, Cambeidge. pp 29–34. https://ui.adsabs.harvard.edu/abs/1996cpd..conf..257B
Bottinga Y, Weill DF (1972) The viscosity of magmatic silicate liquids; a model calculation. Am J Sci 272:438–475. https://doi.org/10.2475/ajs.272.5.438
Chase MW, Davies CA, Downey, Jr. JR, Frurip DJ, McDonald RA, Syverud AN (1985) Phys. Chem. Ref. Data. Suppl. No. 1. In: Chase MW, Davies CA, Downey, Jr. JR, Frurip DJ, McDonald RA, Syverud AN (eds). NIST-JANAF Thermochemical Tables, 3rd edn. American Chemical Society, Washington
Ciesla FJ, Lauretta DS, Hood LL (2004) The frequency of compound chondrules and implications for chondrule formation. Meteorit Planet Sci 39:531–544. https://doi.org/10.1111/j.1945-5100.2004.tb00917.x
Connolly Jr. HC, Jones RH (2016) Chondrules: The canonical and noncanonical views. J Geophys Res Planets 121:1885–1899. https://doi.org/10.1002/2016JE005113
Desch SJ, Connolly Jr. HC (2002) A model of the thermal processing of particles in solar nebula shocks: Application to the cooling rates of chondrules. Meteorit Planet Sci 37:183–207. https://doi.org/10.1111/j.1945-5100.2002.tb01104.x
Desch SJ, Morris MA, Connolly Jr. HC, Boss AP (2012) The importance of experiments: Constraints on chondrule formation models. Meteorit Planet Sci 47:1139–1156. https://doi.org/10.1111/j.1945-5100.2012.01357.x
Distin PA, Hallett GD, Richardson FD (1968) Some reactions between drops of iron and flowing gases. J Iron Steel Inst 206:821–33
Draine BT (2003) Interstellar dust grains. Ann Rev Astron Astrophys 41:241–289. https://doi.org/10.1146/annurev.astro.41.011802.094840
Duchemin L, Popinet S, Josserand C, Zaleski S (2002) Jet formation in bubbles bursting at a free surface. Phys Fluids 14:3000–3008. https://doi.org/10.1063/1.1494072
Ebel DS, Grossman L (2000) Condensation in dust-enriched systems. Geochim Cosmochim Acta 64:339–366. https://doi.org/10.1016/S0016-7037(99)00284-7
Fedkin AV, Grossman L, Ghiorso MS (2006) Vapor pressures and evaporation coefficients for melts of ferromagnesian chondrule-like compositions. Geochim Cosmochim Acta 70:206–223. https://doi.org/10.1016/j.gca.2005.08.014
Fedkin AV, Grossman L, Ciesla FJ, Simon SB (2012) Mineralogical and isotopic constraints on chondrule formation from shock wave thermal histories. Geochim Cosmochim Acta 87:81–116. https://doi.org/10.1016/j.gca.2012.03.020
Fedkin AV, Grossman L (2013) Vapor saturation of sodium: Key to unlocking the origin of chondrules. Geochim Cosmochim Acta 112:226–250. https://doi.org/10.1016/j.gca.2013.02.020
Floss C, El Goresy A, Zinner E, Kransel G, Rammensee W, Palme H (1996) Elemental and isotopic fractionations produced through evaporation of the Allende CV chondrilte: Implications for the origin of hal-type hibonite inclusions. Geochim Cosmochim Acta 60:1975–1997. https://doi.org/10.1016/0016-7037(96)00068-3
Friedrich JM, Weisberg MK, Ebel DS, Biltz AE, Corbett BM, Iotzov IV, Khan WS, Wolman MD (2015) Chondrule size and related physical properties: A compilation and evaluation of current data across all meteorite groups. Geochemistry 75:419–443. https://doi.org/10.1016/j.chemer.2014.08.003
Fujimaki H, Matsu-ura M, Sunagawa I, Aoki K (1981) Chemical compositions of chondrules and matrices in the ALH-77015 chondrite (L3). Mem Natl Inst Polar Res Spec Issue 20:161–174. https://nipr.repo.nii.ac.jp/?action=pages_view_main&active_action=repository_view_main_item_detail&item_id=1211&item_no=1&page_id=13&block_id=104
Fulle M, Marzari F, Della Corte V, Fornasier S, Sierks H, Rotundi A, Barbieri C, Lamy PL, Rodrigo R, Koschny D, Rickman H, Keller HU, López-Moreno JJ, Accolla M, Agarwal J, A'Hearn MF, Altobelli N, Barucci MA, Bertaux J-L, Bertini I, Bodewits D, Bussoletti E, Colangeli L, Cosi M, Cremonese G, Crifo J-F, Da Deppo V, Davidsson B, Debei S, Cecco MD, et al. (2016) Evolution of the dust size distribution of comet 67P/Churyumov–Gerasimenko from 2.2 au to perihelion. Astrophys J 821:19. https://doi.org/10.3847/0004-637x/821/1/19
Georgescu S-C, Achard J-L, Canot É (2002) Jet drops ejection in bursting gas bubble processes. Eur J Mech B/Fluids 21:265–280. https://doi.org/10.1016/S0997-7546(01)01177-3
Giordano D, Russell JK, Dingwell DB (2008) Viscosity of magmatic liquids: A model. Earth Planet Sci Lett 271:123–134. https://doi.org/10.1016/j.epsl.2008.03.038
Gooding JL, Keil K (1981) Relative abundances of chondrule primary textural types in ordinary chondrites and their bearing on conditions of chondrule formation. Meteoritics 16:17–43. https://doi.org/10.1111/j.1945-5100.1981.tb00183.x
Hashimoto A, Kumazawa M, Onuma N (1979) Evaporation metamorphism of primitive dust material in the early solar nebula. Earth Planet Sci Lett 43:13–21. https://doi.org/10.1016/0012-821X(79)90151-1
Hashimoto A (1983) Evaporation metamorphism in the early solar nebula-evaporation experiments on the melt FeO-MgO-SiO_2-CaO-Al_2O_3 and chemical fractionations of primitive materials. Geochem J 3:111–145. https://doi.org/10.2343/geochemj.17.111

Hashimoto A, Nakano Y (2020) Bubbles to Chondrites-II. Chemical fractionations in chondrites. Progress in Earth and Planetary Science, submitted

Hayami S, Toba Y (1958) Drop Production by Bursting of Air Bubbles on the Sea Surface (1) Experiments at Still Sea Water Surface. J Oceanographical Soc Jpn 14:145–150. https://doi.org/10.5928/kaiyou1942.14.145

Hess PC (1977) Structure of silicate melts. Can Mineral 15:162–178. https://pubs.geoscienceworld.org/canmin/article/15/2/162/11155/Structure-of-silicate-melts

Hewins RH (1997) Chondrules. Ann Rev Earth Planet Sci 25:61–83. https://doi.org/10.1146/annurev.earth.25.1.61

Hewins RH, Connolly, Jr. HC, Lofgren GE, Libourel G (2005) Experimental constraints on chondrule formation. In: Krot AN, Scott ERD, Reipurth B (eds). Chondrites and the Protoplanetary Disk. APS, San Francisco. pp 286–316. http://www.aspbooks.org/a/volumes/article_details/?paper_id=2447. Accessed 01 Jul 2020

Hewins RH, Zanda B, Bendersky C (2012) Evaporation and recondensation of sodium in Semarkona type II chondrules. Geochim Cosmochim Acta 78:1–17. https://doi.org/10.1016/j.gca.2011.11.027

Hezel DC, Palme H (2010) The chemical relationship between chondrules and matrix and the chondrule matrix complementarity. Earth Planet Sci Lett 294:85–93. https://doi.org/10.1016/j.epsl.2010.03.008

Hollomon JH, Turnbull D (1953) Nucleation. Prog Met Phys 4:333–388. https://doi.org/10.1016/0502-8205(53)90020-3

Huisman WJ, Peters JF, Zwanenburg MJ, de Vries SA, Derry TE, Abernathy D, van der Veen JF (1997) Layering of a liquid metal in contact with a hard wall. Nature 390:379–381. https://doi.org/10.1038/37069

Ikeda Y, Takeda H (1979) Petrology of the Yamato-74191 Chondrite. Mem Natl Inst Polar Res Spec Issue 12:38–58. https://nipr.repo.nii.ac.jp/?action=pages_view_main&active_action=repository_view_main_item_detail&item_id=958&item_no=1&page_id=13&block_id=104. Accessed 01 Jul 2020

Ikeda Y (1980) Petrology of Allan Hills-764 Chondrites (LL3). Mem Natl Inst Polar Res Spec Issue 17:50–82. https://nipr.repo.nii.ac.jp/?action=pages_view_main&active_action=repository_view_main_item_detail&item_id=1089&item_no=1&page_id=13&block_id=104. Accessed 01 Jul 2020

Ikeda Y (1982) Petrology of the ALH-77003 Chondrite (C3). Mem Natl Inst Polar Res Spec Issue 25:34–65. https://nipr.repo.nii.ac.jp/?action=pages_view_main&active_action=repository_view_main_item_detail&item_id=1378&item_no=1&page_id=13&block_id=104. Accessed 01 Jul 2020

Ikeda Y (1983) Alteration of chondrules and matrices in the four Antarctic carbonaceous chondrites ALH-77307 (C3), Y-790123 (C2), Y-75293 (C2), and Y-74662 (C2). Mem Natl Inst Polar Res Spec Issue 30:93–108. https://nipr.repo.nii.ac.jp/?action=pages_view_main&active_action=repository_view_main_item_detail&item_id=1554&item_no=1&page_id=13&block_id=104. Accessed 01 Jul 2020

Isobe H, Kitamura M, Morimoto N (1986) Volatile-rich chondrules in the Allende meteorite. Mem Natl Inst Polar Res Spec Issue 41:276–286. https://nipr.repo.nii.ac.jp/?action=pages_view_main&active_action=repository_view_main_item_detail&item_id=1970&item_no=1&page_id=13&block_id=104. Accessed 01 Jul 2020

Jarosewich E (1990) Chemical analyses of meteorites: A compilation of stony and iron meteorite analyses. Meteoritics 25:323–337. https://doi.org/10.1111/j.1945-5100.1990.tb00717.x

Jones RH, Scott ERD (1988) The mineralogy of type IA chondrules in Semarkona (LL3.0): Disentangling the igneous and metamorphic histories of type 3 [abstract]. XIX, LPSC:565. https://ui.adsabs.harvard.edu/abs/1988LPI....19..565J/abstract. Accessed 01 Jul 2020

Jones RH (1990) Petrology and mineralogy of type II, FeO-rich chondrules in Semarkona (LL3.0): Origin by closed-system fractional crystallization, with evidence for supercooling. Geochim Cosmochim Acta 54:1785–1802. https://doi.org/10.1016/0016-7037(90)90408-D

Jones RH (1996) FeO-rich, porphyritic pyroxene chondrules in unequilibrated ordinary chondrites. Geochim Cosmochim Acta 60:3115–3117. https://doi.org/10.1016/0016-7037(96)00152-4

Jones RH, Grossman JN, Rubin AE (2005) Chemical, Mineralogical and Isotopic Properties of Chondrules: Clues to Their Origin. In: Krot AN, Scott ERD, Reipurth B (eds). Chondrites and the Protoplanetary Disk. APS, San Francisco. pp 215–285. http://www.aspbooks.org/a/volumes/article_details/?paper_id=2446. Accessed 01 Jul 2020

Kato M (1976) Preparation of Ultrafine Particles of Refractory Oxides by Gas-Evaporation Method. Japan J Appl Phys 15:757–760. https://doi.org/10.1143/jjap.15.757

Kientzler CF, Arons AB, Blanchard DC, Woodcock AH (1954) Photographic Investigation of the Projection of Droplets by Bubbles Bursting at a Water Surface. Tellus 6:1–7. https://doi.org/10.1111/j.2153-3490.1954.tb01085.x

Kimura M, Yagi K, Onuma K (1979) Petrological Studies on Chondrules in Yamato-74 Meteorites. Mem Natl Inst Polar Res Spec Issue 12:114–133. https://nipr.repo.nii.ac.jp/?action=pages_view_main&active_action=repository_view_main_item_detail&item_id=963&item_no=1&page_id=13&block_id=104

Kimura M (1983) Chemical and petrologic relations of the constituent units in ALH-77249 meteorite (L3). Mem Natl Inst Polar Res Spec Issue 30:146–167. https://nipr.repo.nii.ac.jp/?action=pages_view_main&active_action=repository_view_main_item_detail&item_id=1557&item_no=1&page_id=13&block_id=104. Accessed 01 Jul 2020

Kim S-H, Martin PG, Hendry PD (1994) The size distribution of interstellar dust particles. Astrophys J 422:164–175. https://doi.org/10.1086/173714

King EA (1982) Refractory residues, condensates and chondrules from solar furnace experiments [abstract]. XIII, LPSC:389. https://ui.adsabs.harvard.edu/abs/1982LPSC...13..429K/abstract

King EA (1983) Reduction, partial evaporation, and spattering - Possible chemical and physical processes in fluid drop chondrule formation. In: King EA (ed). Chondrules and Their Origins. Lunar and Planetary Institute, Houston. pp 180–187. http://adsabs.harvard.edu/abs/1983chto.conf.....K

Kissel J, Krueger FR (1987) The organic component in dust from comet Halley as measured by the PUMA mass spectrometer on board vega 1. Nature 326:755–760. https://doi.org/10.1038/326755a0

Krot AN, Libourel G, Goodrich CA, Petaev MI (2004) Silica-rich igneous rims around magnesian chondrules in CR carbonaceous chondrites: Evidence for condensation origin from fractionated nebular gas. Meteorit Planet Sci 39:1931–1955. https://doi.org/10.1111/j.1945-5100.2004.tb00088.x

Lambrechts M, Johansen A (2014) Forming the cores of giant planets from the radial pebble flux in protoplanetary discs. Astron Astrophys 572(A107). https://doi.org/10.1051/0004-6361/201424343

Landau LD, Lifshitz EM (1987) Fluid mechanics 2nd ed. In: Course of Theoretical Physics Volume 6. Pergamon Press, Oxford, UK

Lee JS, Weon BM, Park SJ, Je JH, Fezzaa K, Lee W-K (2011) Size limits the formation of liquid jets during bubble bursting. Nat Commun 2:367. https://doi.org/10.1038/ncomms1369

Levison HF, Kretke KA, Walsh KJ, Bottke WF (2015) Growing the terrestrial planets from the gradual accumulation of submeter-sized objects. PNAS 112:14180–14185. https://doi.org/10.1073/pnas.1513364112

Lhuissier H, Villermaux E (2012) Bursting bubble aerosols. J Fluid Mech 696:5–44. https://doi.org/10.1017/jfm.2011.418

Liffman K, Brown M (1995) The motion and size sorting of particles ejected from a protostellar accretion disk. Icarus 116:275–290. https://doi.org/10.1006/icar.1995.1126

Lodders K (2003) Solar system abundances and condensation temperatures of the elements. Astrophys J 591:1220–1247. https://doi.org/10.1086/375492

Lofgren G, Russell WJ (1986) Dynamic crystallization of chondrule melts of porphyritic and radial pyroxene composition. Geochim Cosmochim Acta 50:1715–1726. https://doi.org/10.1016/0016-7037(86)90133-X

MacIntyre F (1972) Flow patterns in breaking bubbles. J Geophys Res 77:5211–5228. https://doi.org/10.1029/JC077i027p05211

Masson CR (1972) Thermodynamics and constitution of silicate slags. J Iron Steel Inst 210:89–96

Nagahara H (1981a) Petrology of chondrules in ALH-77015 (L3) chondrite. Mem Natl Inst Polar Res Spec Issue 20:145–160. https://nipr.repo.nii.ac.jp/?action=pages_view_main&active_action=repository_view_main_item_detail&item_id=1210&item_no=1&page_id=13&block_id=104

Nagahara H (1981b) Evidence for secondary origin of chondrules. Nature 292:135–136. https://doi.org/10.1038/292135a0

Nagashima K, Moriuchi Y, Tsukamoto K, Tanaka KK, Kobatake H (2008) Critical cooling rates for glass formation in levitated Mg_2SiO_4-$MgSiO_3$ chondrule melts. J Mineral Petrol Sci 103:204–208. https://doi.org/10.2465/jmps.070620c

Natta A, Testi L, Calvet N, Henning T, Waters R, Wilner D (2007) Dust in protoplanetary disks: Properties and evolution. In: Reipurth B, Jewitt D, Keil K (eds). Protostars and Planets V. The University of Arizona Press, Tucson. pp 767–781. https://www.lpi.usra.edu/books/PPV/8002.pdf

Nelson LS, Blander M, Skaggs SR, Keil K (1972) Use of a CO_2 laser to prepare chondrule-like spherules from supercooled molten oxide and silicate droplets. Earth Planet Sci Lett 14:338–344. https://doi.org/10.1016/0012-821X(72)90133-1

Nelson SA, Carmichael SE (1979) Partial molar volumes of oxide components in silicate liquids. Contrib Mineral Petrol 71:117–124. https://doi.org/10.1007/BF00375427

Nakamura-Messenger K, Messenger S, Keller LP, Clemett SJ, Zolensky ME (2006) Organic globules in the Tagish Lake meteorite: Remnants of the Protosolar disk. Science 314:1439–1442. https://doi.org/10.1126/science.1132175

O'Dowd CD, Smith MH, Consterdine IE, Lowe JA (1997) Marine aerosol, sea-salt, and the marine sulphur cycle: a short review. Atmos Environ 31:73–80. https://doi.org/10.1016/S1352-2310(96)00106-9

Ott T, Drolshagen E, Koschny D, Güttler C, Tubiana C, Frattin E, Agarwal J, Sierks H, Bertini I, Barbieri C, Lamy PI, Rodrigo R, Rickman H, A'Hearn MF, Barucci MA, Bertaux J-L, Boudreault S, Cremonese G, Da Deppo V, Davidsson B, Debei S, De Cecco M, Deller J, Feller C, Fornasier S, Fulle M, Geiger B, Gicquel A, Groussin O, Gutiérrez PJ, et al. (2017) Dust mass distribution around comet 67p/Churyumov-Gerasimenko determined via parallax measurements using Rosetta's OSIRIS cameras. Mon Not R Astron Soc 469(S276-S284). https://doi.org/10.1093/mnras/stx1419

Pajola M, Lucchetti A, Fulle M, Mottola S, Hamm M, Da Deppo V, Penasa L, Kovacs G, Massironi M, Shi X, Tubiana C, Güttler C, Oklay N, Vincent JB, Toth I, Davidsson B, Naletto G, Sierks H, Barbieri C, Lamy PL, Rodrigo R, Koschny D, Rickman H, Keller HU, Agarwal J, A'Hearn MF, Barucci MA, Bertaux JL, Bertini I, Cremonese G, et al. (2017) The pebbles/boulders size distributions on Sais: Rosetta's final landing site on comet 67p/Churyumov-erasimenko. Mon Not R Astron Soc 469(S636-S645). https://doi.org/10.1093/mnras/stx1620

Poulet F, Lucchetti A, Bibring J-P, Carter J, Gondet B, Jorda L, Langevin Y, Pilorget C, Capanna C, Cremonese G (2016) Origin of the local structures at the philae landing site and possible implications on the formation and evolution of 67p/Churyumov-Gerasimenko. Mon Not R Astron Soc 462(S23-S32). https://doi.org/10.1093/mnras/stw1959

Raizer YP (1960) Condensation of a cloud of vaporized matter expanding in vacuum [english translation]. Sov Phys JETP 37:1229–1235

Rambaldi ER (1981) Relict grains in chondrules. Nature 293:558–561. https://doi.org/10.1038/293558a0

Reed SJB (2005) Electron microprobe analysis and scanning electron microscopy in geology. 2nd edition. Cambridge University Press, Cambridge. https://doi.org/10.1017/CBO9780511610561

Resch FJ, Darrozes JS, Afeti GM (1986) Marine liquid aerosol production from bursting of air bubbles. J Geophys Res Oceans 91:1019–1029. https://doi.org/10.1029/JC091iC01p01019

Resch F, Afeti G (1991a) Gas-liquid conversion at a free interface and its environmental implications. In: Keffer JF, Shah RK, E. N. Grani c (eds). Experimental Heat Transfer, Fluid Mechanics and Thermodynamics. Elsevier, Amsterdam. pp 1066–1076

Resch F, Afeti G (1991b) Film drop distributions from bubbles bursting in seawater. J Geophys Res Oceans 96:10681–10688. https://doi.org/10.1029/91JC00433

Resch, F, Afeti G (1992) Submicron film drop production by bubbles in seawater. J Geophys Res Oceans 97:3679–3683. https://doi.org/10.1029/91JC02961

Richet P, Bottinga Y (1986) Thermochemical properties of silicate glasses and liquids: A review. Rev Geophys 24:1–25. https://doi.org/10.1029/RG024i001p00001

Rietmeijer FJM, Nuth III JA, Karner JM (1999) Metastable eutectic condensation in a Mg-Fe-SiO-H_2-O_2 Vapor: Analogs to Circumstellar Dust. Astrophys J 527:395–404. https://doi.org/10.1086/308080

Rietmeijer FJM, Nuth III JA, Karnerc JM, Hallenbeck SL (2002) Gas-to-solid condensation in a Mg-SiO-H_2-O_2 vapor: metastable eutectics in the MgO-SiO_2 phase diagram. Phys Chem Chem Phys 4:546–551. https://doi.org/10.1039/B103421A

Rietmeijer FJM, Pun A, Nuth III JA (2009) Dust formation and evolution in a Ca-Fe-SiO-H_2-O_2 vapour phase condensation experiment and astronomical implications. Mon Not R Astron Soc 396:402–408. https://doi.org/10.1111/j.1365-2966.2009.14703.x

Rossodivita A, Andreussi P (1999) Spray production by air bubbles bursting on a water surface. J Geophys Res Oceans 104:30059–30066. https://doi.org/10.1029/1999JC900248

Sears DWG, Huang S, Benoit PH (1996) Open-system behaviour during chondrule formation. In: Hewins RH, Jones R, Scott E (eds). Chondrules and the Protoplanetary Disk. Cambridge University Press, Cambridge. pp 221–231. http://adsabs.harvard.edu/abs/1996cpd..conf..221S

Spiel DE (1994) The sizes of the jet drops produced by air bubbles bursting on sea and freshwater surfaces. Tellus B Chem Phys Meteorol 46:325–338. https://doi.org/10.3402/tellusb.v46i4.15808

Spiel DE (1995) On the births of jet drops from bubbles bursting on water surfaces. J Geophys Res Oceans 100:4995–5006. https://doi.org/10.1029/94JC03055

Spiel DE (1997) A hypothesis concerning the peak in film drop production as a function of bubble size. J Geophys Res Oceans 102:1153–1161. https://doi.org/10.1029/96JC03069

Spiel DE (1998) On the births of film drops from bubbles bursting on seawater surfaces. J Geophys Res Oceans 103:24907–24918. https://doi.org/10.1029/98JC02233

Srivastava A, Inatomi Y, Tsukamoto K, Maki T, Miura H (2010) In situ visualization of crystallization inside high temperature silicate melts. J Appl Phys 107:114907. https://doi.org/10.1063/1.3406149

Stebbins JF (1995) Dynamics and structure of silicate and oxide melts; nuclear magnetic resonance studies. In: Stebbins JF, McMillan PF, Dingwell DB (eds). Reviews in Mineralogy and Geochemistry Volume 32. Mineralogical Society of America, Washington D.C. pp 191–246

Stracke A, Palme H, Gellissen M, Münker C, Kleine T, Birbaum K, Günther D, Bourdon B, Zipfel J (2012) Refractory element fractionation in the Allende meteorite: Implications for solar nebula condensation and the chondritic composition of planetary bodies. Geochim Cosmochim Acta 85:114–141. https://doi.org/10.1016/j.gca.2012.02.006

Suzuki T, Mitachi K (1995) Experimental observation of the droplet ejection due to gas bubble bursting at gas liquid interface. Proc 2nd Int Conf Multiphase Flow Kyoto Jpn IP2.3(IP2.9)

Tazzari M, Testi L, Ercolano B, Natta A, Isella A, Chandler CJ, Pérez LM, Andrews S, Wilner DJ, Ricci L, Henning T, Linz H, Kwon W, Corder SA, Dullemond CP, Carpenter JM, Sargent AI, Mundy L, Storm S, Calvet N, Greaves JA, Lazio J, Deller AT (2016) Multiwavelength analysis for interferometric (sub-)mm observations of protoplanetary disks Radial constraints on the dust properties and the disk structure. Astron Astrophys 588(A53). https://doi.org/10.1051/0004-6361/201527423

Toop GW, Somis CS (1962) Some new ionic concepts of silicate slags. Can Metall Q 1:129–152. https://doi.org/10.1179/cmq.1962.1.2.129

Turkdogan ET (1983) Physicochemical properties of molten slags and glasses, Vol. 298. The Metals Society, London. 1–516

Van Schmus WR, Wood JA (1967) A chemical-petrologic classification for the chondritic meteorites. Geochim Cosmochim Acta 31:747–754. https://doi.org/10.1016/S0016-7037(67)80030-9

Vrij A (1966) Possible mechanism for the spontaneous rupture of thin, free liquid films. Discuss Faraday Soc 42:23–33. https://doi.org/10.1039/DF9664200023

Wang J, Davis AM, Clayton RN, Mayeda TK, Hashimoto A (2001) Chemical and isotopic fractionation during the evaporation of the FeO-MgO-SiO_2-CaO-Al_2O_3-TiO_2 rare earth element melt system. Geochimica et Cosmochimica Acta 65:479–494. https://doi.org/10.1016/S0016-7037(00)00529-9

Wasson JT, Krot AN, Lee MS, Rubin AE (1995) Compound chondrules. Geochim Cosmochim Acta 59:1847–1869. https://doi.org/10.1016/0016-7037(95)00087-G

Waters LBFM (2015) Dust in protoplanetary disks: observations. EPJ Web Conf 102:00003. https://doi.org/10.1051/epjconf/201510200003

Wood JA (1988) Chondritic meteorites and the solar nebula. Annu Rev Earth Planet Sci 16:53–72. https://doi.org/10.1146/annurev.ea.16.050188.000413

Wu J (1994) Film drops produced by air bubbles bursting at the surface of seawater. J Geophys Res Oceans 99:16403–16407. https://doi.org/10.1029/94JC01181

Yokokawa T, Niwa K (1969) Free energy and basicity of molten silicate solution. Trans Japan Inst Met 10:81–84. https://doi.org/10.2320/matertrans1960.10.81

Yu Y, Hewins RH, Alexander CMOD, Wang J (2003) Experimental study of evaporation and isotopic mass fractionation of potassium in silicate melts. Geochim Cosmochim Acta 67:773–786. https://doi.org/10.1016/S0016-7037(02)01176-6

Publisher's Note